

# Orbits and action changes during star-clump encounters responsible for the origin of exponential discs in dwarf galaxies

Jian Wu,<sup>1\*</sup> Curtis Struck,<sup>1\*</sup> Bruce G. Elmegreen<sup>2</sup> and Elena D’Onghia<sup>3</sup>

<sup>1</sup>*Department of Physics and Astronomy, Iowa State University, 2323 Osborn Dr., Ames, IA 50011, USA*

<sup>2</sup>*IBM Research Division, T.J. Watson Research Centre, 1101 Kitchawan Road, Yorktown Heights, NY 10598, USA*

<sup>3</sup>*Department of Astronomy, University of Wisconsin-Madison, 475 N Charter St, Madison, WI 53706, USA*

Accepted 2022 September 24. Received 2022 September 18; in original form 2022 July 20

## ABSTRACT

Previous studies found that stellar scattering by massive clumps can lead to the formation of exponential profiles in galaxy discs, but details on how a star is moved around have not been fully explained. We use a GADGET-2 simulation where an exponential profile forms from an initially Gaussian disc in about 4 Gyr for a low-mass galaxy like a dwarf irregular. We find that nearly all large angular momentum changes of stars are caused by star-clump encounters with the closest approach less than 0.5 kpc. During star-clump encounters, stars may increase their random motions, resulting in an increase in the average radial and vertical actions of the whole stellar population. The angular momentum change and the radial action change of an individual star are influenced by the direction from which the star approaches a clump. A star initially at a higher galactic radius relative to the scattering clump usually gets pulled inwards and loses its angular momentum during the encounter, and one at a lower radius tends to shift outwards and gains angular momentum. The increase in the radial action is the largest if a star encounters a clump from the azimuthal direction, and is the smallest from a radial approach. The angular momentum change due to encounters has an inward bias when the clump profile has a steep radial decline, and a shallow decline can make the bias outwards. The stellar profile evolution towards an exponential seems to occur regardless of the direction of the bias.

**Key words:** galaxies: disc – galaxies: evolution – galaxies: kinematics and dynamics

## 1 INTRODUCTION

Galaxies form by the collapse of cosmic filaments with frequent interactions producing their individual angular momenta (Naab & Ostriker 2017). The non-dissipative component of this collapse, e.g., dark matter, ends up in a thick halo and the dissipative component, initially gas, forms a disc. Star formation in this gas builds up a stellar disc over time, with high turbulent speeds at the earliest stages forming a thick stellar disc (Elmegreen & Elmegreen 2006), which is still faintly visible as old stars in galaxies today (Burstein 1979), and gradually decreasing turbulence forming a thin disc that dominates their visual appearance in optical images (Yoachim & Dalcanton 2006). During most of this process, the stellar disc has an exponential radial profile, i.e., in both the thick and the thin components (Comerón et al. 2012), although there is often an upward or downward break in this profile with an exponential on either side (Pohlen & Trujillo 2006; Bouquin et al. 2018; Staudaher et al. 2019). The fundamental origin of this exponential form is unclear. Explanations range from the initial collapse profile (Mestel 1963; Freeman 1970) to disc viscosity (Lin & Pringle 1987) to spiral (Sellwood & Binney 2002) or bar (Hohl 1971) torques, but

all of these have problems (Ferguson & Clarke 2001; Daniel & Wyse 2018), or are not universally applicable (Elmegreen & Struck 2013), which is a key feature of galaxy exponentials. For example, models that rely on shear for viscosity or magnetic torques might not work in dwarf irregular galaxies, which have low shear yet extensive exponential stellar profiles (Herrmann et al. 2013).

Point scattering of stars can make the radial exponential profile (Elmegreen & Struck 2013; Elmegreen et al. 2014; Elmegreen & Struck 2016; Struck & Elmegreen 2017a,b, 2019) at the same time as it increases the stellar velocity dispersion, e.g., by cloud scattering, as in the proposal by Spitzer & Schwarzschild (1951). Studies of the dispersion alone (e.g., Wielen 1977) cannot predict the radial dependence of the scattered stars. To study the radial dependence without additional complications that arise in a real galaxy, other disc processes such as gravitational interactions between individual stars and spiral density waves (Shu 2016), were removed in several of our previous papers, leaving only non-interacting stars to scatter off co-orbiting mass perturbations. In these papers, the result always converged to an exponential stellar disc in about one Gyr.

While scattering alone makes physical and mathematical sense for the origin of galaxy exponentials, the ultimate test is a fully self-gravitating  $N$ -body simulation of a galaxy with a live disc and halo, as that will include all of the dynamical processes that develop

\* E-mail: jianwu@iastate.edu (JW), curt@iastate.edu (CS)

simultaneously, such as density waves. In simulations using the GADGET-2 code (Springel 2005), Wu et al. (2020) started with a non-exponential stellar profile and artificially added 200 point masses to drive the scattering. These point masses had a mass of  $7.3 \times 10^6 M_\odot$  and were identified with giant interstellar cloud complexes close to the maximum mass of Galactic molecular clouds (Williams & McKee 1997). The initial vertical profile was assumed to be the equilibrium solution for an isothermal layer,  $\text{sech}^2(z/z_0)$ , for vertical coordinate  $z$  and scale height  $z_0$ . After slightly less than one billion years, the radial profile of the stellar disc always evolved to a form of  $e^{-r/h}/r$ , which is indistinguishable from an exponential beyond one scale length. The timescale was shorter for a less radially stable disc, i.e., a lower Toomre parameter (Toomre 1964),  $Q$ , and for more massive clouds. At the same time as the exponential formed in surface density, the velocity dispersion in the  $z$ -direction also developed an exponential radial profile with about twice the scale length of the surface density. This factor of 2 results in a nearly constant disc thickness, as also observed (van der Kruit & Searle 1981) but never explained previously. In this model, disc evolution stops when the gas is gone.

All of these experiments including the full  $N$ -body simulations gave exponential discs, but questions about how the orbital radius of each star changes or why the changes lead to an exponential were not examined. Wu et al. (2020) showed that a close encounter between a star and a clump is able to modify the angular momentum of the star, but did not indicate how much of the angular momentum change was caused by encounters.

Another interesting question is whether point scattering of stars exhibits a radial bias. If a bias exists, one may also ask what affects its direction and its strength. Elmegreen & Struck (2016) showed stochastic scattering in a disc with a constant inwards bias leads to an equilibrium near-exponential stellar profile. However, it is not clear that an inwards bias is required for the formation of an exponential if non-equilibrium states are acceptable.

In this paper, we try to fill the gaps described above and analyze star-clump encounters in detail. In Section 2, we introduce an  $N$ -body simulation similar to the fiducial one of Wu et al. (2020) but with modifications to further suppress unwanted perturbations in the initial disc. We also present a local shearing sheet model to study orbits during encounter events. In Section 3, we show results from the galaxy simulation, including the profile evolution of the stellar disc, statistics of large stellar angular momentum changes, the connection between these changes and star-clump encounters, and action changes of stars during close encounters with clouds. Detailed explanations of these changes, based on properties of orbital action, are provided in Section 4. Also in this section we illustrate the orbits during star-clump encounters and use the orbits to understand angular momentum changes and radial action changes of stars. We further show that the direction of scattering bias is related to the clump density distribution in the disc. A summary and conclusions are given in Section 5.

## 2 MODEL

In this section, we explain properties of our  $N$ -body simulations, methods used to calculate stellar actions, and the rotating frame in which star-clump encounters are studied by a set of differential equations for orbits in a shearing sheet.

### 2.1 Simulations

Wu et al. (2020) showed, using a  $N$ -body simulations, that galactic discs can evolve to an exponential due to star-clump interactions. To study the physical mechanisms responsible for the disc evolution, we set up a simulation using initial conditions similar to the fiducial run of Wu et al. (2020), but with a few modifications.

In the simulation, the total mass of our galaxy is  $1.45 \times 10^{11} M_\odot$ , with 98% of the total mass in the dark matter halo and 2% in the stellar disc. The number of particles representing the dark matter and stars are  $4 \times 10^6$  and  $1 \times 10^6$  respectively. The profile of the dark matter halo is a Hernquist (1990) profile, and the density distribution satisfies the following:

$$\rho_{\text{dm}}(r) = \frac{M_{\text{dm}}}{2\pi} \frac{a}{r(r+a)^3}, \quad (1)$$

where  $M_{\text{dm}}$  is the total mass of the halo and the Hernquist constant  $a$  is set to 13.8 kpc. The initial density profile of the stellar disc is an isothermal distribution in the vertical direction and a Gaussian distribution in radius described by

$$\rho_{\text{star}}(r, z) = \frac{M_{\text{star}}}{2\pi z_0 h^2} \text{sech}^2\left(\frac{z}{z_0}\right) e^{-r^2/h^2}, \quad (2)$$

where  $M_{\text{star}}$  is the total mass of the stellar disc, the scale length  $h$  is set to 5.4 kpc, and the scale height  $z_0$  is set to 0.45 kpc. The scale length for the Gaussian corresponds to a smaller effective scale length for an exponential equivalent: if we consider a disc at 4 exponential scale lengths, where the surface density is  $\exp(-4)$  times the central value, this position corresponds to a radius for the Gaussian where  $(r/h)^2 = 4$ , which means that the equivalent exponential scale length is  $r/4 = 0.5h$ , or 2.7 kpc. This is a fairly small galaxy, consistent with the stellar mass (see below) of  $1.45 \times 10^9 M_\odot$ . The disc scale height of 0.45 kpc is consistent with the large ratios of thickness to length in dwarf irregular galaxies, where Hunter & Elmegreen (2006) found an average ratio of  $\sim 0.5$  for 94 dIrrs. Initially, there are no clumps in the model.

This model galaxy is evolved without clumps for 2.94 Gyr under the control of the  $N$ -body package GADGET-2, designed by Springel (2005). Without clumps, little evolution occurs in the profile of the stellar disc during this time. The purpose of the 2.94 Gyr is to let the disc settle down from the initial conditions. A specific goal is to let ring waves in the stellar disc, due to initial imperfect centripetal balance, gradually die out.

At 2.94 Gyr, we reduce the mass of all the star particles by one half, and then randomly select 210 of these particles to have their mass increased to  $7.3 \times 10^6 M_\odot$ . We henceforth identify these particles as clumps (similar to D'Onglia et al. 2013). At this point, the total mass of all the clumps is roughly the same as the total mass of the stars, and the density profile of clumps is the same as that of stars as well. Like the stars, the clumps have a relatively large scale height, which is typical for the interstellar media of low-mass galaxies (Dalcanton et al. 2004).

We run the galaxy with GADGET-2 for another 5.88 Gyr. In this period, stars interact with clumps, and the stellar profile changes significantly. When referring to time  $T$  elapsed in the simulation, we measure it from the beginning of this period. The stellar profile at  $T = 0$  is shown in Figure 1. The Toomre  $Q$  profile at  $T = 0$  and the component and total rotation curves at  $T = 0$  are shown in Figures 2 and 3, respectively.

A parameter comparison between this simulation and the fiducial run in Wu et al. (2020) is summarized in Table 1. A significant change is that dark matter mass is increased here in order to stabilize the stellar disc against spontaneous spiral waves and wavelets in-

duced by the clumps. Since these waves also scatter stars, the large halo mass suppresses their effect on stellar orbits and makes star-clump interactions that we want to study more pronounced. Related to this change is an increase in the average value of the Toomre  $Q$  parameter (Fig. 2) compared to our previous work. The high value of  $Q$  (see Fig. 2) in the numerical experiments reduces the gravitational response of the disk to perturbations. Modest disk self-gravity also prevents wavelets from amplifying around the clumps (Julian & Toomre 1966; D’Onghia et al. 2013). N-body simulations of low-mass disks, perturbed by clumps and with lower  $Q \approx 1.3$ , were shown in D’Onghia et al. (2013). In those experiments, the disc started with an exponential shape so major structural changes could not be observed, the clumps were not allowed to move radially so they could not transfer their own angular momentum to stars, and the clumps were lower mass than in the present simulations. As a result, the structural parameters of the stellar disk did not change over time and there was no significant stellar heating as in the present simulations (see also Vera-Ciro et al. (2014)).

Other parameters related to stars and clumps in this work are roughly the same as in Wu et al. (2020), except the initial shape of clump density profile. We will discuss the effect of this profile later in the paper. For parameters that are not explicitly listed in the table, we use the same values as Wu et al. (2020). For example, gravitational softening lengths used in the model for dark matter, stars, and clumps are 0.2 kpc, 0.1 kpc, and 0.1 kpc, respectively. These values are identical to Wu et al. (2020).

## 2.2 Action calculation

To investigate the time evolution of stellar orbits, we study the angle-action variables. Actions are generally conserved integrals in fixed potentials, so their changes reflect perturbations in the stellar motions. The actions convenient to use in an axisymmetric potential are the radial action, vertical action, and azimuthal action. The specific radial action of a star is defined as

$$J_r = \frac{1}{2\pi} \iint_V dr dv_r, \quad (3)$$

where  $r$  and  $v_r$  are the radial position and the radial velocity of the star, and  $V$  is the enclosed region of the stellar orbit in phase space. Similarly, the specific vertical action is defined as

$$J_z = \frac{1}{2\pi} \iint_V dz dv_z, \quad (4)$$

where  $z$  and  $v_z$  are the vertical position and the vertical velocity of the star. The specific azimuthal action is simply the  $z$ -component of the specific angular momentum of the star (see Section 3.5 of Binney & Tremaine 2008), i.e.,

$$J_\phi = L_z. \quad (5)$$

The GADGET-2 simulation generates positions and velocities of stars and clumps every 1.96 Myr. The actions of a star at a given moment are calculated based on its position, its velocity, and the galaxy potential at the moment, using the AGAMA software library developed by Vasiliev (2019). Technically, the actions are path integrals around the whole of an orbit. The instantaneous actions from the AGAMA code can be interpreted as path integrals around a hypothetical orbit derived from the instantaneous position and velocity of a star. The AGAMA library assumes that stellar orbits are integrable, and approximates the galaxy potential with a best fitting Stäckel potential when calculating the actions. This method is called ‘Stäckel fudge’ (Binney 2012). The AGAMA

function `ActionFinder` is specially called to produce radial actions, vertical actions, and azimuthal actions. We compared the specific azimuthal actions obtained from `ActionFinder` with the  $z$ -components of specific angular momenta  $L$ , calculated by

$$\mathbf{L} = \mathbf{r} \times \mathbf{v}, \quad (6)$$

where  $\mathbf{r}$  represents positions and  $\mathbf{v}$  represents velocities. The difference is typically less than 1 per cent. We will consider the results of these action calculations in Sec. 3.3.

## 2.3 Motions of stars in a rotating frame: shearing sheet model

In the GADGET-2 simulation, the ensemble of stars experience a slight change of orbital angular momentum on average when massive clouds are present. The reason for this loss is that individual stars change their angular momentum just because they interact with the clumps. Higher order effects may include or be related to a non-uniform clump density profile, orbital geometry in the local region of a star-clump encounter, scattering with a clump binary or ternary, a velocity dispersion gradient in the stars, and other factors. To figure out the dominant factor, we also study star-clump encounters in a simplified model, assuming that the galaxy potential produces a flat rotation curve at all radii. We assume clumps rotate about the galactic centre in perfect circular orbits on the midplane of the galaxy and are not influenced by gravity from a star. When a star approaches a clump, the star feels a gravitational force from the clump and the force due to the galaxy potential gradient. We assume the clump has a galactic radius  $R_0$ , and the constant circular speed of the galaxy is  $v_0$ .

To study the motion of the star, we choose a rotating frame centred on the clump with the  $x$ - $y$  plane coinciding with the midplane of the galaxy.  $\mathbf{e}_x$  is along the radial direction of the galaxy, pointing away from the galactic centre.  $\mathbf{e}_y$  points towards the direction of galaxy rotation at the location of the clump. The angular velocity  $\boldsymbol{\Omega}_0$  of this frame in the inertial frame is  $\Omega_0 \mathbf{e}_z$ , where the angular speed  $\Omega_0$  satisfies

$$\Omega_0 = \frac{v_0}{R_0}. \quad (7)$$

In the rotating frame, the coordinate of the galactic centre is  $(-R_0, 0, 0)$ . The equation of motion of the star is

$$\frac{d^2 \mathbf{x}}{dt^2} = -\nabla \Phi - \nabla \Phi_{\text{clump}} - 2\boldsymbol{\Omega}_0 \times \frac{d\mathbf{x}}{dt} - \boldsymbol{\Omega}_0 \times (\boldsymbol{\Omega}_0 \times (\mathbf{x} + \mathbf{p})), \quad (8)$$

where  $\mathbf{x} = (x, y, z)$  is the coordinate of the star in the rotating frame,  $\Phi$  is the galaxy potential,  $\Phi_{\text{clump}}$  is the gravitational potential of the clump,  $\mathbf{p} = (R_0, 0, 0)$  is a constant vector which makes the coordinate transition from the rotating frame centred on the clump to a rotating frame with the origin at the galactic centre. Since the model galaxy has a constant circular speed, the galaxy potential gradient on the midplane satisfies

$$\nabla \Phi = \frac{v_0^2}{|\mathbf{x} + \mathbf{p}|} \frac{\mathbf{x} + \mathbf{p}}{|\mathbf{x} + \mathbf{p}|}, \quad (9)$$

which gives

$$\nabla \Phi|_x = \frac{v_0^2}{|\mathbf{x} + \mathbf{p}|} \frac{x + R_0}{|\mathbf{x} + \mathbf{p}|}, \quad (10)$$

$$\nabla \Phi|_y = \frac{v_0^2}{|\mathbf{x} + \mathbf{p}|} \frac{y}{|\mathbf{x} + \mathbf{p}|}. \quad (11)$$

**Table 1.** Parameter comparison between the model in this paper and the fiducial run in [Wu et al. \(2020\)](#)

Parameters	Values in this paper	Values in <a href="#">Wu et al. (2020)</a>
Total mass $M_{\text{tot}}$	$1.45 \times 10^{11} M_{\odot}$	$2.9 \times 10^{10} M_{\odot}$
Dark matter mass $M_{\text{dm}}$	$1.42 \times 10^{11} M_{\odot}$ (98% $M_{\text{tot}}$ )	$2.6 \times 10^{10} M_{\odot}$ (90% $M_{\text{tot}}$ )
Star mass $M_{\text{star}}$	$1.45 \times 10^9 M_{\odot}$ (1% $M_{\text{tot}}$ )	$1.45 \times 10^9 M_{\odot}$ (5% $M_{\text{tot}}$ )
Clump mass $M_{\text{clump}}$	$1.52 \times 10^9 M_{\odot}$ (1% $M_{\text{tot}}$ )	$1.45 \times 10^9 M_{\odot}$ (5% $M_{\text{tot}}$ )
Number of dark matter particles $N_{\text{dm}}$	4 000 000	970 000
Number of star particles $N_{\text{star}}$	999 790	1 000 000
Number of clumps $N_{\text{clump}}$	210	200
Individual star mass $M_{\text{star}}/N_{\text{star}}$	$1.45 \times 10^3 M_{\odot}$	$1.45 \times 10^3 M_{\odot}$
Individual clump mass $M_{\text{clump}}/N_{\text{clump}}$	$7.3 \times 10^6 M_{\odot}$	$7.3 \times 10^6 M_{\odot}$
Dark halo Hernquist constant $a$	13.8 kpc	8.05 kpc
Initial scalelength of the stellar disc $h$	5.4 kpc	5.4 kpc
Initial scale height of the stellar disc $z_0$	0.45 kpc	0.45 kpc
initial shape of clump density profile	$e^{-r^2/h^2}$	$\frac{1}{\sqrt{r}}$

The clump potential gradient satisfies

$$\nabla\Phi_{\text{clump}} = \frac{Gm_{\text{clump}}}{|\mathbf{x}|^2} \frac{\mathbf{x}}{|\mathbf{x}|}, \quad (12)$$

where  $m_{\text{clump}}$  is the mass of individual clump, and  $G$  is the gravitational constant. We constrain the motion of the star to the midplane of the galaxy, so the  $z$  component of galactic gravity is ignored. Equation 8 then reduces to two-dimensions and becomes the following:

$$\frac{d^2x}{dt^2} = -\frac{v_0^2(x+R_0)}{(x+R_0)^2+y^2} - \frac{Gm_{\text{clump}}x}{(x^2+y^2)^{3/2}} + 2\Omega_0 \frac{dy}{dt} + \Omega_0^2(x+R_0), \quad (13)$$

$$\frac{d^2y}{dt^2} = -\frac{v_0^2y}{(x+R_0)^2+y^2} - \frac{Gm_{\text{clump}}y}{(x^2+y^2)^{3/2}} - 2\Omega_0 \frac{dx}{dt} + \Omega_0^2y. \quad (14)$$

These are the differential equations for the the local shearing sheet model.

In Equations 13 and 14,  $v_0$  is set to  $113 \text{ km s}^{-1}$ , which is the rotation speed of the outer disc in the GADGET-2 simulation;  $m_{\text{clump}}$  is  $7.3 \times 10^6 M_{\odot}$ , which is the mass of an individual clump. A gravitational softening length  $s$  of 0.1 kpc is added to the denominator of the second term on the right-hand-side of Equations 13 and 14, so the denominator becomes  $(x^2+y^2+s^2)^{3/2}$  instead of  $(x^2+y^2)^{3/2}$ . This softening length is the same as the softening length used in GADGET-2; the purpose here is to model the extended size of a cloud. To obtain the trajectory of a star, Equations 13 and 14 are solved numerically, using an explicit Runge-Kutta (4,5) formula ([Dormand & Prince 1980](#); [Shampine & Reichelt 1997](#)). Specifically, the ode45 function provided by MATLAB is employed.

### 3 RESULTS FROM THE GALAXY SIMULATION

#### 3.1 Time evolution of the simulated galaxy disc

Before presenting the results from our analysis of orbits, we show in this subsection the macroscopic changes of the simulated disc with time, and compare it with the fiducial run in [Wu et al. \(2020\)](#).

Figure 1 shows the time evolution of the surface density profile of the stellar disc. At  $T = 0$ , the stellar disc has a Gaussian profile with a few ring waves outside of  $R = 10$  kpc. Later on, these ring waves die out, and the profile within  $R = 10$  kpc evolves to a nearly straight line, which represents an exponential disc. At  $T = 6$ , the

whole disc is a Type II exponential with a small overdense region at the galactic centre.

This profile evolution confirms the formation of an exponential disc out of star-clump scattering as seen in [Wu et al. \(2020\)](#). Since the initial clump distribution used here is different from that of [Wu et al. \(2020\)](#), this evolution result also indicates that the profile change towards an exponential through star-clump scattering happens with various clump density distributions. However, the clump distribution can affect the scalelength of the exponential formed. When comparing the final stellar profile with that of [Wu et al. \(2020\)](#), a difference is that the density profile has a steeper slope or a smaller scalelength than [Wu et al. \(2020\)](#) in the region outside of  $R = 10$  kpc. This can be explained by the clump density distinction. As shown in Table 1, [Wu et al. \(2020\)](#) used a  $1/\sqrt{r}$  clump radial profile, while the run in this paper has an  $e^{-r^2/h^2}$  profile. The number of clumps in the latter decreases with increasing radius faster than the former. Therefore, fewer clumps are outside of  $R = 10$  kpc, compared with the former run. Owing to limited star-clump interaction, the stellar profile in this paper has little change outside of  $R = 10$  kpc despite the disappearance of ring waves.

We also recall that a model with a flat initial density profile was described in [Wu et al. \(2020\)](#). Other initial profiles were tested in unpublished models. Qualitatively, the profile evolution towards an exponential form is not changed by these different initial conditions.

To better quantify how closely a profile fits an exponential, we calculate the second derivative of the logarithmic density profile with respect to the radius  $R$ , and then take the average value from  $R = 2$  to  $R = 9$  kpc. When computing the second derivative, we firstly divide the disc into concentric annuli, each with a width of 1 kpc. Secondly, the number of stars in every annulus is counted and then used to calculate the surface density of the annulus. Thirdly, the logarithm of the surface density is calculated and the second derivative at the radius of the annulus is approximated by  $(\ln\Sigma(r+\delta r) + \ln\Sigma(r-\delta r) - 2\ln\Sigma(r-\delta r))/\delta r^2$ , where the step  $\delta r$  is 1 kpc. From  $R = 2$  to  $R = 9$  kpc, the values of the second derivative may fluctuate, but usually have the same sign. For a perfect exponential profile, the logarithm of the radial density equals  $-r/h$ , and the second derivative of this is 0. For a Gaussian profile with  $e^{-r^2/h^2}$ , the logarithm of the radial density is  $-r^2/h^2$ , and the second derivative is  $-2/h^2$ . Here, the initial stellar disc is a Gaussian with  $h = 5.4$  kpc, so the theoretical second derivative is  $-0.069 M_{\odot} \text{ pc}^{-2} \text{ kpc}^{-2}$ . Figure 4 shows the time evolution of the second derivative for the simulated stellar disc. The initial value

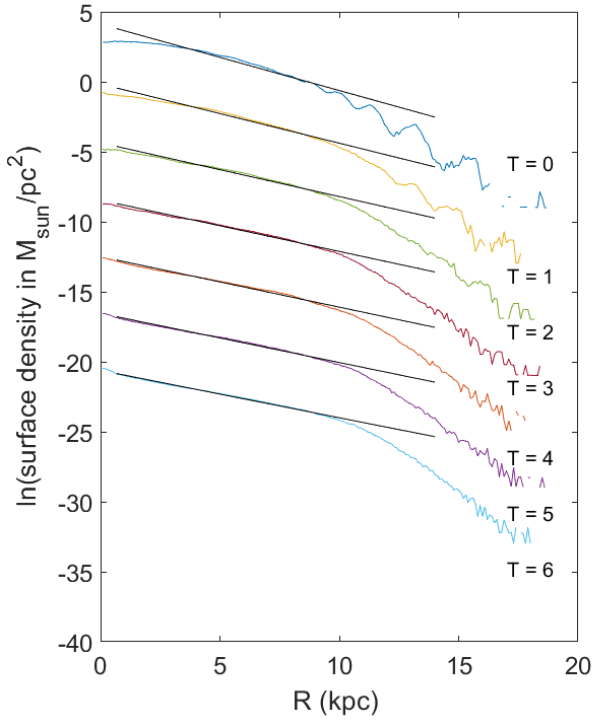


**Figure 1.** Evolution of the stellar surface density profile in the simulated galaxy. Except for  $T = 0$ , curves are offset downwards successively by 4 units to give clear views. Black lines are the lines of best fit in the interval of  $[2, 10]$  kpc. The R-squared of the linear fitting from  $T = 0$  to  $T = 6$  are 0.9759, 0.9835, 0.9849, 0.9906, 0.9873, 0.9929, and 0.9943, respectively. The root mean squared error of the fitting from  $T = 0$  to  $T = 6$  in units of the vertical axis are 0.174, 0.128, 0.111, 0.084, 0.096, 0.069, and 0.060, respectively. When using the slope of the best fit line to determine an exponential scale length, the effective scale length from  $T = 0$  to  $T = 6$  are 2.11, 2.36, 2.60, 2.73, 2.77, 2.85, and 2.96 kpc, respectively. The time unit used in this plot is 0.98 Gyr.

is around  $-0.07 M_{\odot} \text{pc}^{-2} \text{kpc}^{-2}$ , which agrees with the theoretical calculation. After a transitory drop, the second derivative increases steadily and reaches  $-0.02 M_{\odot} \text{pc}^{-2} \text{kpc}^{-2}$  at 5.88 Gyr. The change of the second derivative towards 0 verifies that the disc is gradually turning into an exponential profile. The effective exponential scale length at 5.88 Gyr is 2.96 kpc, and smaller at earlier times. The plot also shows that the rate of change is fast during the first 2 Gyrs, and slows down afterwards. When we analyze stellar orbits later in this paper, we will focus on dynamics in the first 2 Gyrs.

Figure 5 shows the time evolution of the stellar velocity dispersions in the  $r$ -direction and  $z$ -direction measured at a galactic radius of 5 kpc (i.e., over a range of 4.75-5.25 kpc). The  $r$ -dispersion goes from  $14 \text{ km s}^{-1}$  to  $25 \text{ km s}^{-1}$ , and the  $z$ -dispersion goes from  $12 \text{ km s}^{-1}$  to  $18 \text{ km s}^{-1}$ . The shape of the two curves resembles the fiducial run in Wu et al. (2020). As we will see later in this paper, the increased random motion in the  $r$ -direction and the  $z$ -dispersion can be explained by star-clump encounters.

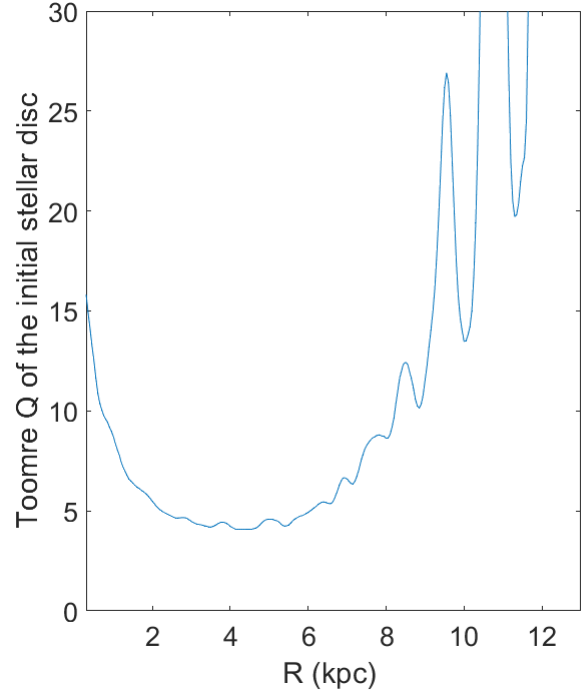


**Figure 2.** Toomre Q of the stellar disc at  $T = 0$ . The oscillation in the curve beyond  $R = 8$  kpc is due to ring waves in stellar density.

### 3.2 Stellar angular momentum change in the simulated galaxy

The change of the stellar density profile seen in Figure 1 is a collective effect of numerous changes in the orbital radius of individual stars. To understand the main causes of the stellar profile change, we study angular momentum changes of individual stars.

Changes in angular momentum of individual stars are evaluated in time windows with a duration of 196 Myr. A series of time windows, successively shifted by 19.6 Myr, is observed. Within a time window, the change in specific angular momentum is defined as the difference between the maximum and the minimum angular momenta, and the time for this angular momentum change is defined as the average of the two time points when the maximum and the minimum occur. We say a change in specific angular momentum is large when the value of the change is greater than  $75 \text{ kpc km s}^{-1}$ . Given the rotation velocity of  $115 \text{ km s}^{-1}$  in the outer part of the stellar disc, this large specific angular momentum change indicates a radial shift of more than 0.65 kpc for a star.

In the simulated galaxy, the angular momenta of 9903 random stars are tracked. Figure 6 shows the distribution of the closest distance of a tracked star to any of the clumps in a time window during which the tracked star has a large angular momentum change. The normalized frequency peaks at 0.1 kpc. When adding up the bins where the closest distance is less than 0.5 kpc, a probability of 0.973 is obtained. This indicates that 97.3% of the large stellar angular momentum changes are associated with clump encounters with a distance less than 0.5 kpc. Therefore, close star-clump encounters are the main cause of stellar angular momentum changes in the simulated galaxy.

In the first 1 Gyr of disc evolution, large angular momentum changes occur 11974 times for the 9903 stars. On average, each

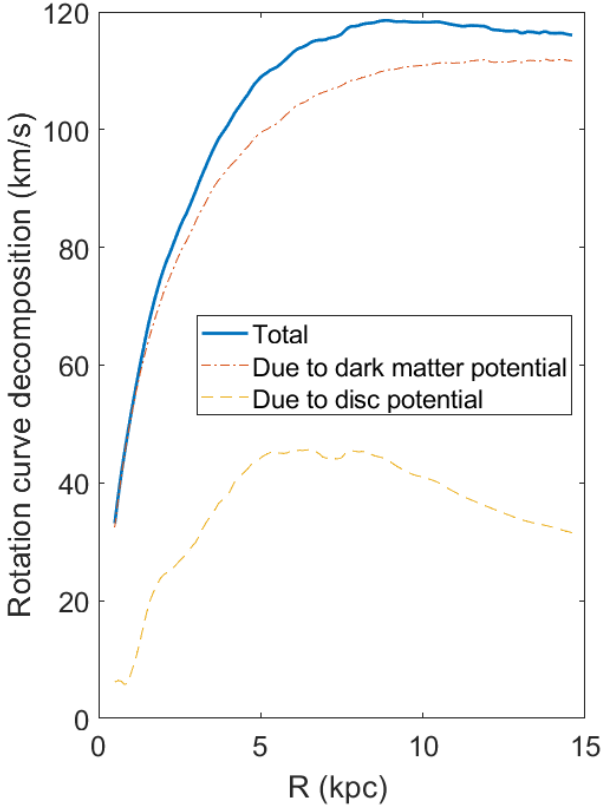


**Figure 3.** Azimuthally averaged rotation curve of the disc at  $T = 0$ . The solid blue curve shows the rotational speeds on the galaxy midplane. The dash-dotted orange curve and the dashed yellow curve give contribution due to dark matter potential gradient and disc potential gradient, respectively.

star experiences a large change 1.2 times in the first 1 Gyr. The stars lose angular momentum in 49.23% of the cases and gain in 50.77%, so moving radially outwards after a clump encounter is slightly favoured. However, this result is not statistically supported at a significance level of 0.05. Take a null hypothesis to be that the probability of gaining angular momentum is 0.5, and the alternative hypothesis to be that the probability is not equal to 0.5. Considering the sample size and assuming the mean probability follows a normal distribution by applying the central limit theorem, the  $p$ -value of the hypothesis testing is 0.094. Because the  $p$ -value is greater than 0.05, the null hypothesis is not rejected. This means that the probability of gaining or losing angular momentum could be 50%, without a bias in one direction or the other. The topic on the radial bias of angular momentum changes will be discussed in detail later in this paper.

Figure 7 shows the frequency of large angular momentum changes in the radial interval from 2 to 9 kpc as a function of time from 0.2 Gyr to 1.8 Gyr. The bin width of the figure is 19.6 Myr. The plot has a large fluctuation near 1 Gyr, but exhibits an overall downward trend. (At this time the clumps are well distributed throughout the stellar disc, and thus, close to a maximum number of stars. At other times, the clumps are more clumped, and thus, close to fewer stars. Although large, this is essentially a statistical fluctuation.) The downward trend qualitatively matches the rate of stellar profile changes shown on Figure 4. When the frequency of

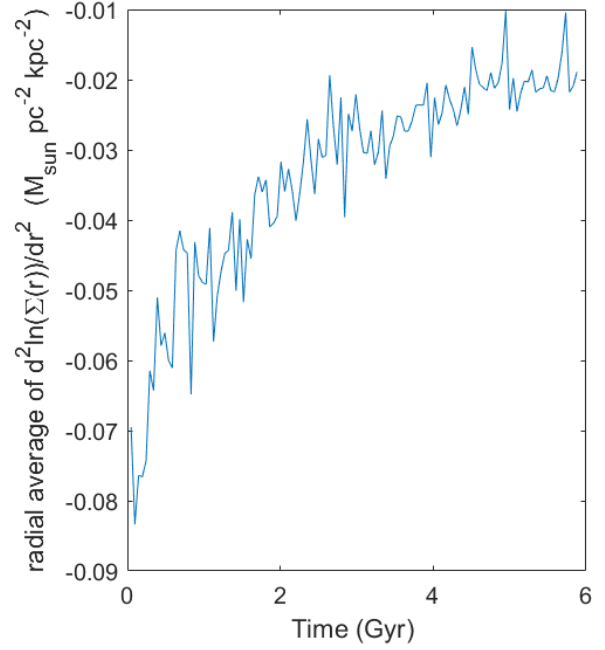


**Figure 4.** Time evolution of the second derivative of the logarithm radial stellar profile. The radial average is taken from 2 kpc to 9 kpc.

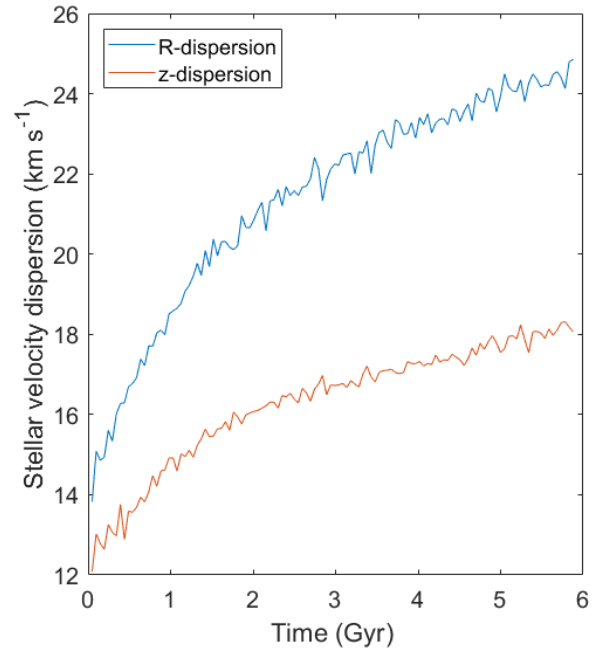


**Figure 5.** Time evolution of stellar velocity dispersions in the  $r$ -direction and  $z$ -direction. The velocity dispersions at each time point are valued at the galactic radius of 5 kpc.

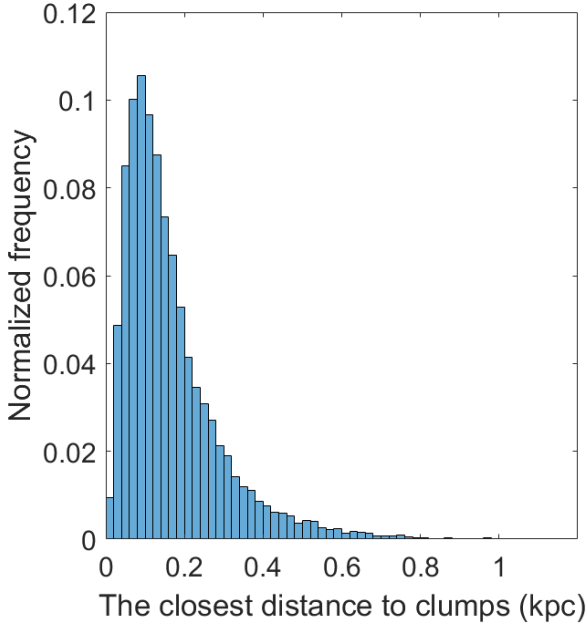


**Figure 6.** Distribution of the closest distance to any clumps during a 196 Myr time window when a star experiences a  $L_z$  change greater than  $75 \text{ kpc km s}^{-1}$ . The width of a bin in the plot is 0.02 kpc.

large  $L_z$  changes decreases with time, the profile evolution slows down.

### 3.3 Action changes during star-clump encounters

In the previous subsection, we showed that the closest star-clump encounters are responsible for nearly all of the large  $L_z$  changes in the simulation. This is true even with the softening parameter equal to 0.1 kpc for the cloud interactions. In this subsection, we focus on the influence of these encounters on stellar action integrals.

In the simulated galaxy, trajectories of 9903 random stars are tracked with a high time resolution. We say a close encounter event occurs if any of the tracked stars enters the neighbourhood of any of the 210 clumps. Here, we define the neighbourhood of a clump as the three-dimensional sphere centred on the clump with a radius of 0.5 kpc. In the first 1 Gyr, 276 711 encounter events are detected for all the tracked stars. On average, each star experiences encounter events 27.9 times. This is much more than the frequency of large  $L_z$  changes shown in the previous subsection. A large  $L_z$  change is almost certainly caused by a close encounter, but an encounter may not produce a large  $L_z$  change. Also note that a star can reside in the neighbourhood of more than one clump simultaneously. In this scenario, we count the event multiple times based on the number of clumps involved. Encounters with multiple clumps usually happen in the central region of the disc, since the clump density there is high.

Table 2 shows mean stellar action changes during one star-clump encounter at different radial locations in the first 1 Gyr. The action changes are calculated using the values when the star enters and leaves a clump neighbourhood. The galactic radii in the table are radii of stars, evaluated when the stars go into the clump neighbourhood. The last column in the table shows the average number of encounters experienced in 1 Gyr per star. As the clump

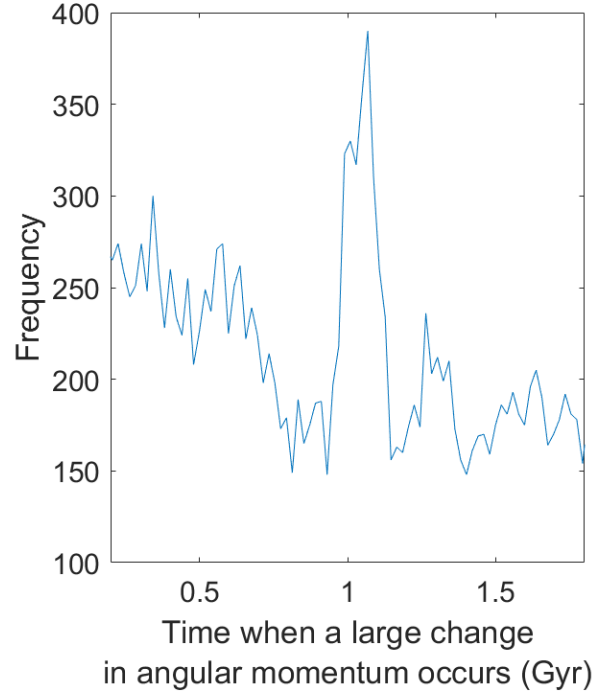


**Figure 7.** The frequency of large  $L_z$  changes for 9903 tracked stars as a function of time from 0.2 Gyr to 1.8 Gyr. The bin width in the horizontal direction is 19.6 Myr.

surface density peaks at the galactic center, the average number of encounters per star increases as the galactic radius goes down. Although the mean action changes in one star-clump interaction have a small magnitude, frequent encounters can lead to a big effect.

From 1 kpc to 6 kpc, the mean  $L_z$  change is negative, indicating that encounters are more likely to make a star lose  $L_z$  and move inwards after meeting with a clump. This movement leads to an increase in stellar density in the disc centre, and eventually drives the formation of a central cusp as seen in Figure 1 at  $T = 6$ . From 7 kpc to 10 kpc, the uncertainty in  $L_z$  change is comparable to the absolute value. Therefore, the radial bias is not statistically significant. This agrees with the null hypothesis in the previous subsection. Large  $L_z$  changes studied before are ones with changes of more than  $75 \text{ kpc km s}^{-1}$ . (Note: the  $L_z$  changes in Table 2 are averaged over all stars, not just those with large changes.) They are unlikely to occur in the inner disc, because the rotation velocity there is low and a star has to radially migrate by a long distance to meet the criterion of  $75 \text{ kpc km s}^{-1}$ . The previous statistics on large  $L_z$  changes mostly reflect scattering in the outer disc.

As shown in the table, the mean  $J_r$  and  $J_z$  changes are all positive, and the values of changes generally increase with galactic radii. This means that encounters with clumps, on average, intensify the random motion of stars in the  $r$ -direction and  $z$ -direction. It also explains the rises in the velocity dispersion seen in Figure 5.

To better understand the action changes during encounters, we classify encounter events based on clump incoming angles. The definition of a clump incoming angle is shown in Figure 8. The left panel of the figure shows a face-on view of a local region in the galactic disc. The red cross and the blue dot represents the locations of a star and a clump, respectively. This local frame is centred on the star, downwards is the direction to the galactic centre, and left

**Table 2.** Mean action changes of a star during one encounter with a clump at different Galactic radii in the GADGET-2 run. An action change is calculated using the action value when a star enters a sphere of 0.5 kpc radius around the clump and the one when the star goes out of the sphere. The galactic radius is the distance of the star to the galactic centre, evaluated at the moment when the star goes into the sphere.

Galactic radius (kpc)	Mean $L_z$ change (kpc km s $^{-1}$ )	Mean $J_r$ change (kpc km s $^{-1}$ )	Mean $J_z$ change (kpc km s $^{-1}$ )	Average number of encounters experienced in one gigayear per star
1	$-0.18 \pm 0.03$	$0.09 \pm 0.01$	$0.07 \pm 0.01$	77.6
2	$-0.49 \pm 0.04$	$0.06 \pm 0.01$	$0.11 \pm 0.01$	51.4
3	$-0.51 \pm 0.06$	$0.13 \pm 0.01$	$0.11 \pm 0.01$	35.2
4	$-0.41 \pm 0.09$	$0.23 \pm 0.01$	$0.13 \pm 0.01$	26.6
5	$-0.62 \pm 0.14$	$0.30 \pm 0.02$	$0.19 \pm 0.01$	16.6
6	$-0.70 \pm 0.25$	$0.34 \pm 0.03$	$0.26 \pm 0.02$	9.4
7	$-0.45 \pm 0.42$	$0.41 \pm 0.05$	$0.34 \pm 0.03$	6.2
8	$-0.48 \pm 0.72$	$0.64 \pm 0.07$	$0.55 \pm 0.05$	3.4
9	$-0.64 \pm 1.35$	$0.88 \pm 0.14$	$0.69 \pm 0.08$	1.6
10	$-4.65 \pm 3.20$	$1.05 \pm 0.28$	$0.90 \pm 0.15$	0.6

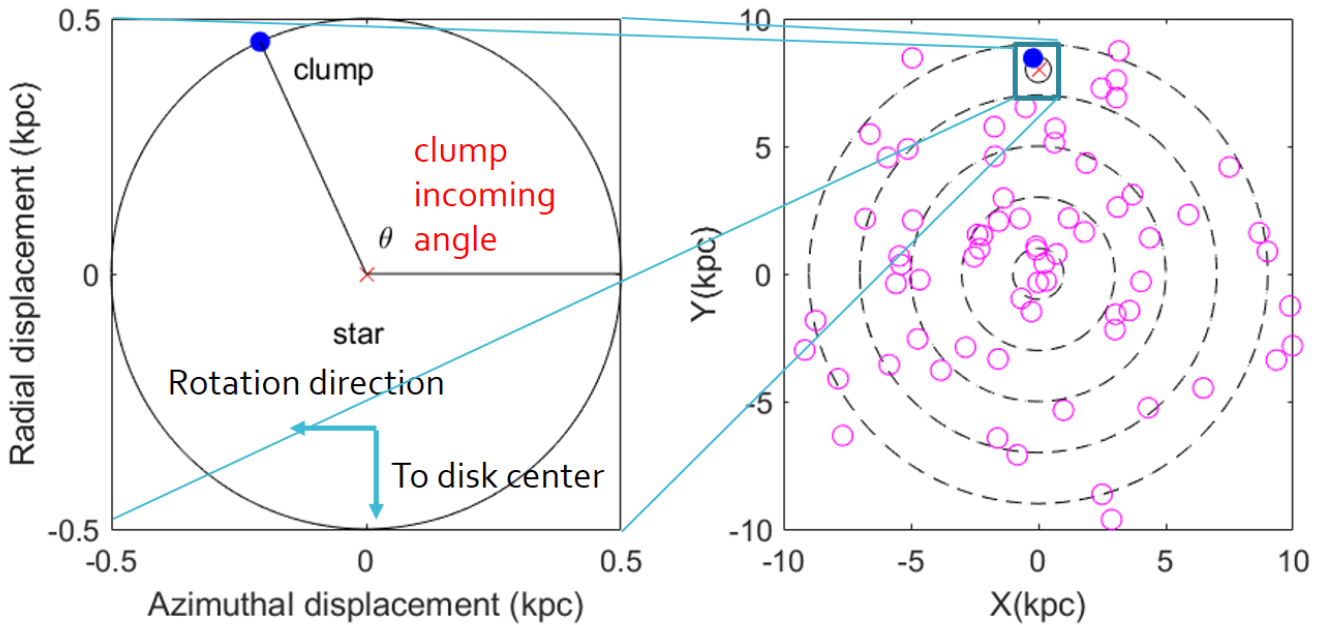


**Figure 8.** A demonstration of the definition of a clump incoming angle. Assume a star, represented by a red cross, enters the neighbourhood of a clump represented by a blue dot. The left panel shows a local reference frame centred on the star where the galactic centre is at the downward direction and the direction of disc rotation is the left. The clump incoming angle is the angular displacement of the clump in this frame, shown as the angle  $\theta$  on the plot. The black circle has a radius of 0.5 kpc. If the clump has the same  $z$ -coordinate as the star when the star enters its neighbour, the clump will be on the circle as shown here. Otherwise, it will be inside the circle. If the star is at the galactic radius of 8 kpc, right panel shows the positions of the star and the clump along with the black circle in the global frame taking the galactic centre as the origin. Magenta dots in the plot represents other clumps in the galaxy. Concentric circles, added for clarity, are at 1 kpc, 3 kpc, 5 kpc, 7 kpc, and 9 kpc. The galaxy rotates counterclockwise on this panel. The clump population shown on the plot is for demonstration purpose only, and does not reflect the clump density profile in the simulation.

is the direction of disc rotation. This frame, with the heavy clumps orbiting past the light, but fixed star, is somewhat counter-intuitive initially, but it is the natural frame for the present calculations. We will use a clump-centred frame in other discussions below. When a star enters the neighbourhood of a clump, the clump will be on or inside the 0.5 kpc circle shown in the figure. The clump incoming angle  $\theta$  is defined as the angle measured counterclockwise from the right as shown in the figure. Specifically, if the clump approaches the star from below (negative  $y$ -value in the figure), then the angle span is measured clockwise and we define the clump incoming angle as a negative value. That is, we consider an angular range of from  $-180^\circ$

to  $+180^\circ$ . Thus in general, if a clump incoming angle is positive, the clump comes with a galactic radius greater than the star, but if the angle is negative, the clump comes with a galactic radius less than the star. The right panel of the figure shows the position of star-clump encounter region on the disc plane if the galactic radius of the star is 8 kpc. In this panel, the origin is the disc centre and the disc rotates counterclockwise. Magenta dots represent other clumps in the galaxy.

In Figure 9, the left panel shows the distribution of clump incoming angles for encounter events occurring at different galactic radii. The right panel shows the average  $L_z$  change of the encoun-

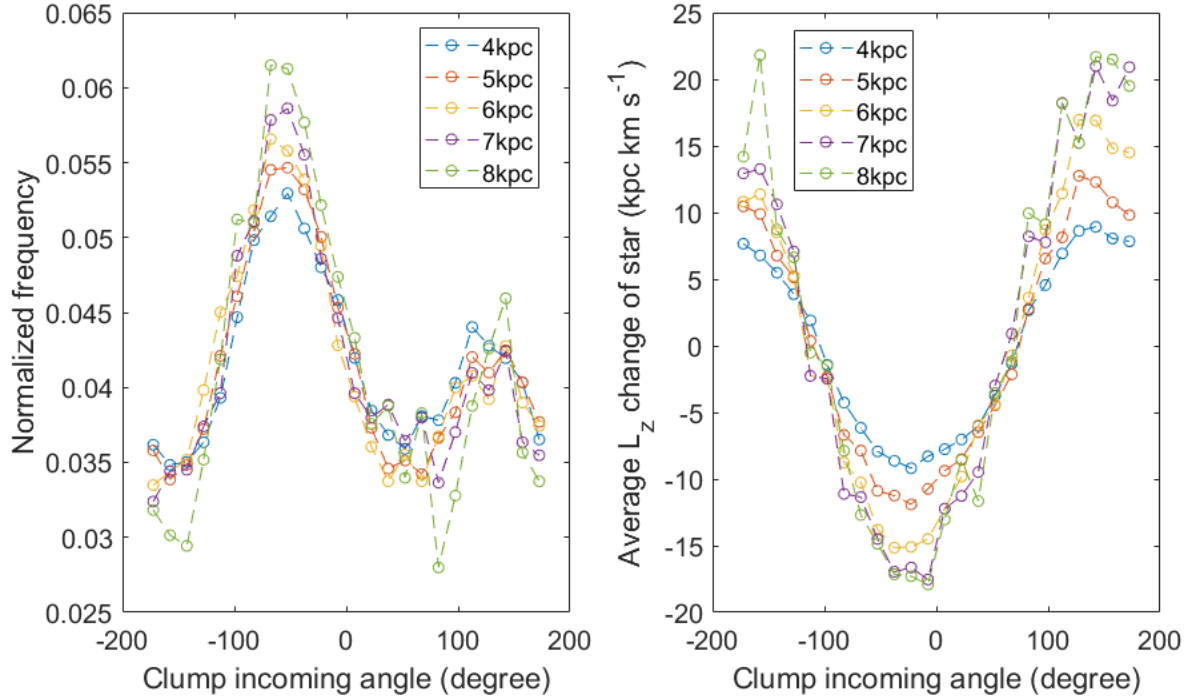


**Figure 9.** The distribution of clump incoming angles and average  $L_z$  changes as a function of clump incoming angles in star-clump collisions. Colors reflect encounters occurring at different galactic radii. The bin width in both panels is 15 degrees.

ters that belong to the same incoming angle bin. The width of the angle bins is 15 degrees. We show encounters from 4 kpc to 8 kpc (over the first 2.0 Gyr), because this region has a sufficiently large encounter sample and does not greatly suffer from encounters involving multiple clumps.

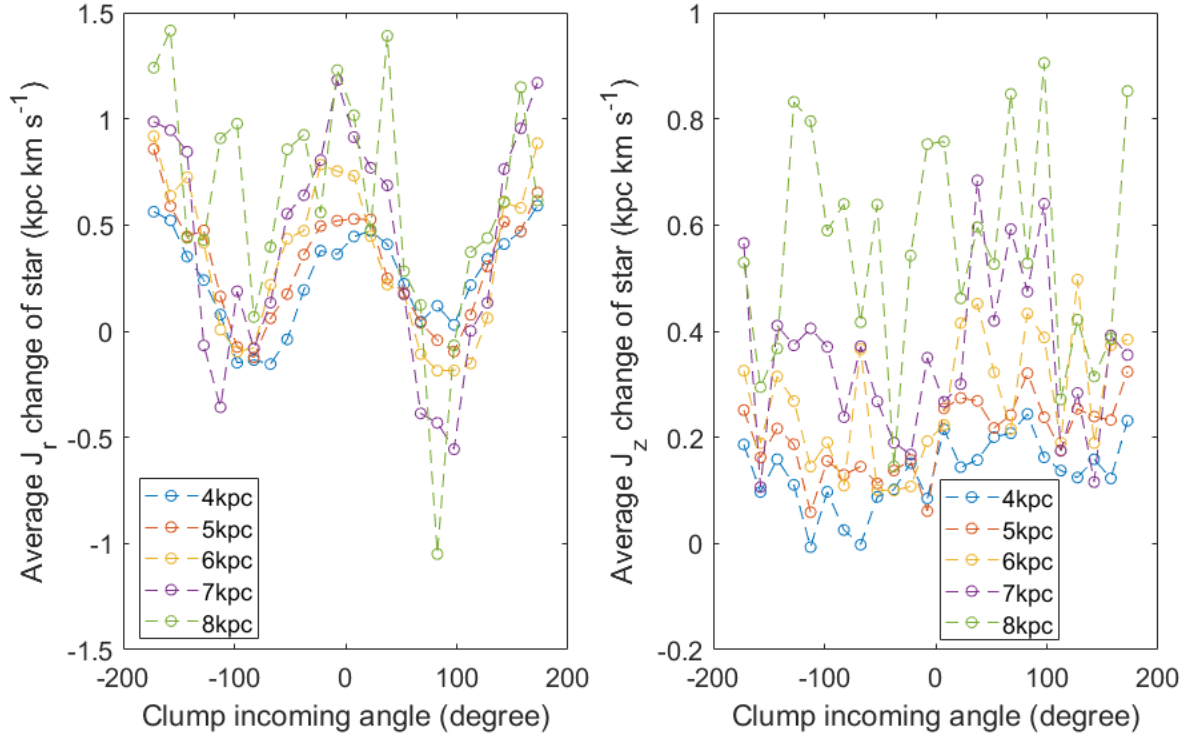
Curves on the left panel overlap and give two crests and two troughs. This can be explained by the differential rotation of the disc. Assume a star and a clump rotate about the galactic centre in circular orbits. If the clump has a greater orbital radius than the star, it will have a smaller angular velocity. The encounter with the star will occur when the star catches up with it, and this will lead to a clump incoming angle between  $90^\circ$  and  $180^\circ$ . If the clump has a smaller orbital radius than the star, it will have a greater angular velocity. The encounter will occur when it overtakes the star, and this gives a clump incoming angle between  $-90^\circ$  and  $0^\circ$ . The angle intervals  $[-180^\circ, -90^\circ]$  and  $[0^\circ, 90^\circ]$  are forbidden under the assumption of circular orbits. When the star and the clump have some random energy in the radial direction, the two forbidden intervals can get filled, and this occurs in the two troughs on the plot.

Curves on the right panel also manifest a clear shape. Encounters with the clump incoming angle between  $-105^\circ$  and  $75^\circ$  lose  $L_z$  on average, and the rest of the angles gain. When the star and the clump have low orbital energy in random motion, the trajectory of the star in the neighbourhood of the clump can be inferred given a clump incoming angle, and the  $L_z$  change of the star can be determined from the trajectory. As a result, there is a direct connection between the clump incoming angle and the  $L_z$  change for near-circular orbits. Clumps that come in between  $-105^\circ$  and  $75^\circ$  initially have a lower orbital radius than the star and end up with a higher orbital radius, passing behind the star in azimuth. This pulls

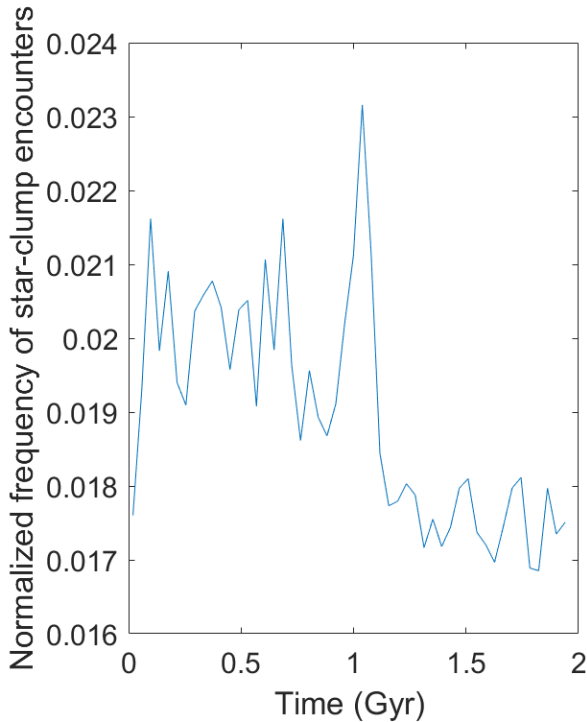
the star back in its orbit and causing it to lose angular momentum. We will discuss this more in the next section.

Figure 10 shows  $J_r$  and  $J_z$  changes as a function of clump incoming angle. The  $J_r$  plot reveals a shape of "W" with the troughs around  $-90^\circ$  and  $90^\circ$ . Similar to  $L_z$ , the  $J_r$  changes can be estimated by using the trajectory of the star on the disc plane, so they are related to clump incoming angles. We will see this in detail later. The  $J_z$  changes are positive and show little dependence on clump incoming angle. This makes sense because  $J_z$  is associated with motions in the  $z$ -direction and clump incoming angles give no information on that. When examining  $J_z$  changes by using motions in the  $z$ -direction, one will find that the cause of  $J_z$  changes shares a similar nature with the  $J_r$  changes. We will not specifically discuss  $J_z$  evolution in this paper.

Figure 11 shows the frequency of star-clump encounters as a function of time. As mentioned earlier, an encounter involving multiple clumps simultaneously will be counted multiple times. To reduce the effect of multiple counting, we select only encounters occurring at a galactic radius greater than 2 kpc when making the plot. In the figure, the normalized encounter frequency has a downward trend, and a large fluctuation happens around 1 Gyr. These features match up with what we see in Figure 7. When the encounter frequency goes down, so does the large  $L_z$  change frequency. This confirms that star-clump encounters generate stellar  $L_z$  changes. The downward trend in Figure 11 may be caused by increased random motion in the  $z$ -direction. When the stellar disc gets thicker, the separation between stars and clumps in the  $z$ -direction increases, and the chance of a star entering the three-dimensional neighbourhood of a clump goes down.



**Figure 10.** Average  $J_r$  and average  $J_z$  changes as a function of clump incoming angles. Colors reflect encounters occurring at different galactic radii. The bin width in both panels is 15 degrees.



**Figure 11.** Normalized frequency of star-clump encounters as a function of time from 0 to 1.96 Gyr. Only encounters that occur at a galactic radius greater than 2 kpc are counted. The width of a bin is 39.2 Myr.

#### 4 STAR-CLUMP ENCOUNTERS IN THE LOCAL SHEARING SHEET MODEL

In the previous section, we showed the stellar profile evolution towards an exponential, suggested that the large  $L_z$  changes are caused by close star-clump encounters, and illustrated statistics on action integral changes during encounter events. Particularly, we presented the distribution of clump incoming angles and demonstrated a dependence of  $L_z$  and  $J_r$  changes on these angles. To dig deeper into the shape of the distribution curve and the explanation of the dependence, we use the local shearing sheet model. As mentioned in Section 2.3, the local shearing sheet model depicts the trajectory of a star under the influence of a clump on a perfectly circular orbit, on top of an axisymmetric galaxy potential with a flat rotation curve.

##### 4.1 Stellar orbits in the clump neighbourhood

In this subsection, we try to understand the dependence of  $L_z$  and  $J_r$  changes of clump incoming angles. Before investigating this issue, let us look at stellar orbits during an encounter in the local shearing sheet model. Assume a star is initially in a perfect circular orbit at a galactic radius  $r_0 = 8$  kpc. We set the rotational velocity  $v_0$  in the model to be  $113 \text{ km s}^{-1}$ , which is the value in the galaxy simulation, so we can compare results with the simulation later. A clump is placed about 1 kpc away from the initial position of the star in the azimuthal direction. The galactic radius  $R_0$  of the clump can vary from 7 kpc to 9 kpc with an increment of 0.1 kpc. The galactic radius  $R_0$  of the clump affects whether the star can enter the neighbourhood of the clump at a later time. Figure 12 shows the stellar orbit in a rotating frame centred on the clump for the

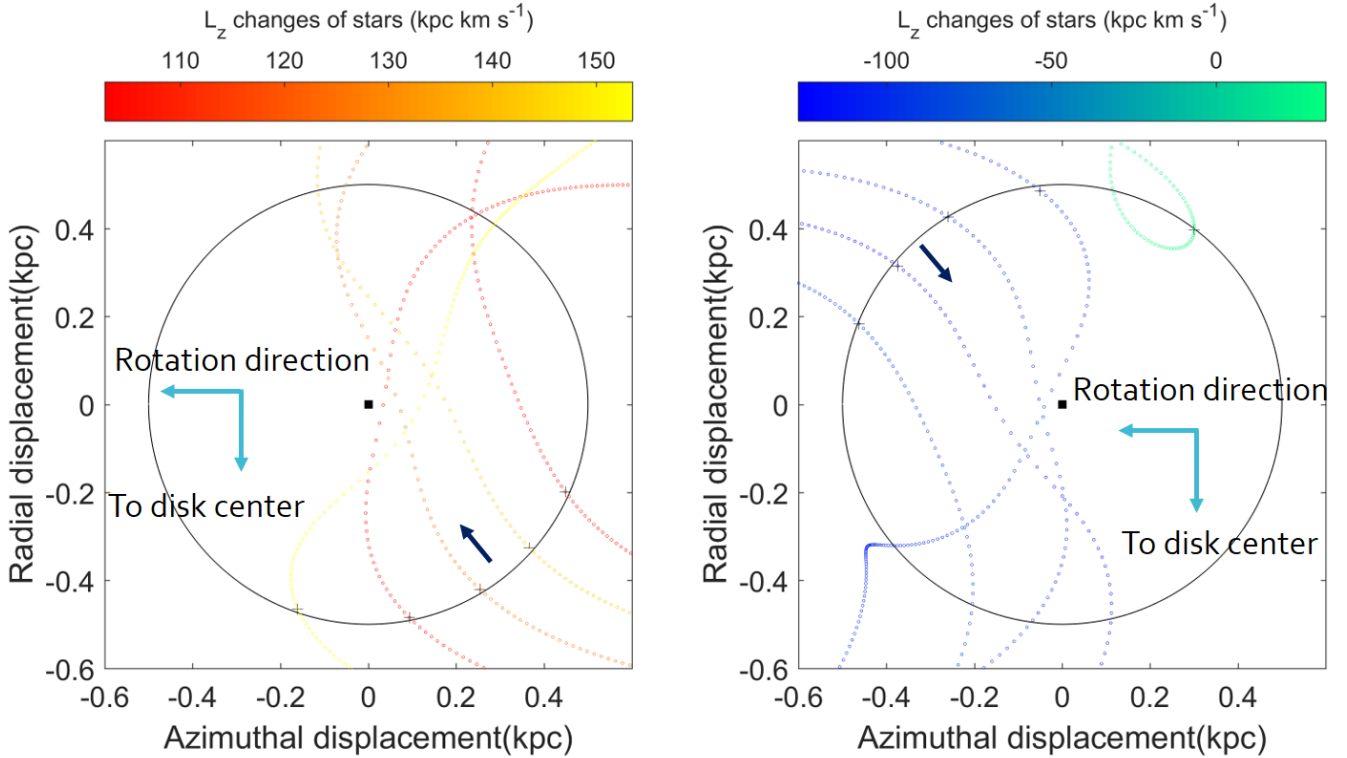


**Figure 12.** Face-on view of stellar orbits in the rotating frame centred on the clump, produced in the local shearing sheet model. The black square in the centre is the position of the clump. Dotted curves are positions of the stars observed every 1.96 Myr. A star initially moves in a circular orbit at 8 kpc. Black plus signs mark the positions where the star enters the clump neighbourhood. Black arrows show the direction of stellar motions in this frame. On each panel, downwards is the direction to the galactic centre, and left is the direction of disc rotation. The left panel shows the cases where the clump is initially placed ahead of the star in the azimuthal direction by roughly 1 kpc. In this panel, the five stellar tracks ordered by their plus signs from right to left correspond to clump galactic radii  $R_0$  of 8.4, 8.5, 8.6, 8.7, 8.8 kpc, respectively. The right panel shows the cases where the clump is initially placed behind the star in the azimuthal direction by roughly 1 kpc. The five stellar tracks ordered by their plus signs from left to right correspond to clump galactic radii  $R_0$  of 7.6, 7.5, 7.4, 7.3, 7.2 kpc, respectively. The color of dotted curves indicates the  $L_z$  change of the star, measured by using the values when the star enters and leaves the clump neighbourhood.

cases where the star goes into the clump neighbourhood. The black square at the centre of each panel is the position of the clump. The black circles have a radius of 0.5 kpc. Dotted curves are tracks of the star in the neighbourhood of the individual clump realizations (superposed in a common ‘clump frame’ in the figure). The time difference between two dots is 1.96 Myr. Black plus signs on the black circle are locations where the star enters the circle. From these signs, one can tell the direction of stellar motions. The color of the dotted curve indicates the  $L_z$  change of the star from the circle entrance point to the circle exit point. In each panel, downwards is the direction to the galactic centre, and left is the direction of disc rotation. The left panel shows the cases where the star is initially placed behind of the clump in the azimuthal direction, so the star tracks come in from the lower right. In this panel, the five stellar tracks ordered by their plus signs from right to left correspond to clump galactic radii  $R_0$  of 8.4, 8.5, 8.6, 8.7, 8.8 kpc, respectively. Recall that the star is always at 8 kpc radius, so the stellar tracks that start furthest in radius (y-coordinate) from the clump correspond to clump positions furthest from 8 kpc. Although the coordinate of the clump is (0,0) for all cases on this local frame of reference, the site of the clump in the galactic disc is different for each case. The right panel shows the scenarios where the clump is initially placed behind the star in the azimuthal direction. The five stellar tracks

ordered by their plus signs from left to right correspond to clump galactic radii  $R_0$  of 7.6, 7.5, 7.4, 7.3, 7.2 kpc, respectively.

When the clump has a galactic radius greater than that of the initial star (left panel of Figure 12), the star approaches the clump from a lower galactic radius and then gets thrown outwards to a higher radius. The stellar trajectory in the rotating frame bends before it passes the clump, so the trajectory does not go around the clump. When the clump has a galactic radius less than the star, the star meets the clump from a higher galactic radius and then gets sent inwards to a lower radius in front of the clump with a decrease in the  $L_z$ , except for  $R_0 = 7.2$  kpc which barely intercepts the clump interaction radius. These trajectories from above also do not go around the clump. The stellar paths in the figure agree with orbits in Figure 8.12 of Binney & Tremaine (2008). The orbits of stars in Binney & Tremaine (2008) bend before they pass the mass point when their initial galactic radii have a small difference from the mass point. When the difference in galactic radii gets large, Figure 8.12 in Binney & Tremaine (2008) also shows a trajectory where the star reverses its motion in the radial direction, as does the  $R_0 = 7.2$  kpc case in our right panel.

To understand the  $L_z$  change of a star during an encounter, we need to figure out the torque exerted on the star by the gravity of the clump. The magnitude of the torque depends on the strength

of the gravity and its direction relative to the disc rotation. To better examine the torque from the clump, the position of the clump during an encounter is presented in a moving frame centred on the star. On the stellar moving frame, at each time point, we create a Cartesian coordinate system with the origin at the position of the star. Its horizontal and vertical axes are along the azimuthal and radial directions at the star, respectively.

Figure 13 shows the positions of the clump in this moving frame for orbits in Figure 12. In Figure 13, the black pentagram at the centre of each panel is the position of the star in this local frame. The black circles have a radius of 0.5 kpc. In each panel, downwards is the direction to the galactic centre, and left is the direction of disc rotation. Dotted curves are positions of the clump. When a star enters the neighbourhood of the clump, it can be viewed from the perspective of the star as the clump entering the star neighbourhood. Black crosses mark the entrance points where the clump goes into the circle. They are also used to determine the clump incoming angles. The colors of the dotted curves show the  $L_z$  changes of the star as before.

On the left panel, the five tracks ordered by their entrance points from left to right correspond to clump galactic radii  $R_0$  of 8.4, 8.5, 8.6, 8.7, 8.8 kpc, respectively. The clump incoming angles are  $159.3^\circ$ ,  $140.9^\circ$ ,  $122.9^\circ$ ,  $101.5^\circ$ , and  $69.8^\circ$ , respectively. The  $L_z$  changes of the star are 102.7, 142.7, 125.0, 104.0, and 153.5, in units of  $\text{kpc km s}^{-1}$ . In this panel, as the clump galactic radius  $R_0$  increases, the clump incoming angle goes down until the star cannot enter the clump neighbourhood. On the right panel, the five tracks ordered by their entrance points from right to left correspond to clump galactic radii  $R_0$  of 7.6, 7.5, 7.4, 7.3, 7.2 kpc, respectively. The clump incoming angles are  $-25.0^\circ$ ,  $-42.9^\circ$ ,  $-60.6^\circ$ ,  $-84.4^\circ$ , and  $-124.9^\circ$ , respectively. The  $L_z$  changes of the star are -97.3, -126.8, -105.3, -105.5, and 33.2, in unit of  $\text{kpc km s}^{-1}$ . Here, as the clump galactic radius  $R_0$  falls, the clump incoming angle decreases until the star cannot enter the clump neighbourhood.

In Figure 13, when the position of the clump is in the second or third quadrant, the torque from clump gravity on the star is positive. When the clump position is in the first or fourth quadrant, the torque is negative. The magnitude of the torque is higher if the clump has a smaller distance to the star or the direction from the star to the clump is closer to the azimuthal axis. For any orbit in the left panel, most clump positions are in the second or third quadrant. Since the angular momentum change is the time integral of the torque, the  $L_z$  changes in this panel are all positive. In the right panel, the track of  $R_0 = 7.2$  kpc has clump positions in the third quadrant, so the  $L_z$  change is positive. For the rest of orbits, most clump positions are in the first or fourth quadrant, so their  $L_z$  changes are negative.

We can also use clump positions in Figure 13 to explain the  $J_r$  changes of the star, although  $J_r$  changes are a little more complicated. When the clump is in the first or second quadrant in Figure 13, the gravity from the clump on the star has an outward radial component, and this component will generate an outward impulse on the radial motion of the star as time goes on. When the clump is in the third or fourth quadrant, gravity will produce an inward impulse on the star. If the outward impulse is greater than the inward impulse, the star receives a net outward impulse. Otherwise, it receives a net inward impulse. The  $J_r$  change of the star depends not only on the direction of the net impulse received, but also on the phase of the radial motion when the star enters the clump neighbourhood. If the star is initially moving outwards in the radial direction or has an outwards momentum, a net outward impulse will increase its radial action and a net inward impulse will reduce it. If the star is initially moving inwards, the change of  $J_r$  is the opposite. If the star does

not initially have any random motion in the radial direction, a net impulse regardless of its direction will increase the  $J_r$  of the star. In Figure 13, the track with a clump incoming angle of  $101.5^\circ$  is roughly symmetric about the azimuthal axis across the star. The magnitude of the outward impulse due to clump positions in the first and second quadrants is close to the magnitude of the inward impulse from the third and fourth quadrants. Therefore, the net impulse is very small, which means the  $J_r$  change should also be small. The track with an incoming angle of  $159.3^\circ$  has most of the clump positions in the third quadrant. The net impulse should be relatively large, since most of the clump positions contribute to the impulse in the same radial direction. In the simulated galaxy, the radial velocity dispersion of stars is much less than the rotational velocity in the outer disc. Usually we can assume that the radial actions of stars before encounter events are negligible there. Therefore, a large net impulse at the angle of  $159.3^\circ$  indicates a big  $J_r$  change. These results agree with the  $J_r$  change curve in Figure 10. In Figure 10, the  $J_r$  change at the angle of  $101.5^\circ$  is close to 0, and the change at  $159.3^\circ$  is around the peak value.

Now let us look at encounter orbits in the simulated disc at the galactic radius of 8 kpc. There are two major differences between the simulated disc and the local shearing sheet model. First, neither clumps nor stars in the galaxy simulation move in perfect circles. Their orbits can carry random energy in the radial or azimuthal direction. Second, clumps and stars can have velocity components perpendicular to the galaxy midplane. When a star meets a clump, their  $z$ -coordinates may not be the same.

Figure 14 shows the clump paths in the moving frame of the star for encounters at 8 kpc in the simulated galaxy. The left panel shows encounters with the clump incoming angle of  $120^\circ$  and the right panel shows encounters with the incoming angle of  $-60^\circ$ . Again, downwards is the direction to the galactic centre, and left is the direction of disc rotation. The time difference between two successive dots on a track is 1.96 Myr, the same as the value used in the local shearing sheet model. The color of a track tells the  $L_z$  change of the star during the encounter. As one can see, some clump tracks do not start or end at the boundary of the 0.5 kpc circle. This is because the clump and the star do not have the same  $z$ -coordinate at the moment when the star enters or leaves the clump neighbourhood and the projected position of the star's impact on the neighbourhood sphere is inside the sphere's projected circle.

In the left panel of Figure 14, most of the clump paths do not go around the star at the centre. This is what the local shearing sheet model predicts. However, three curves do go around the star before they reverse their motion in the radial direction, due to non-zero random motions. The  $L_z$  changes for these paths are negative, which is the opposite of the other paths. This means that the torque from the clump at the closest approach dominates the change in  $L_z$  of the star. When the clump path envelops the star, the clump position at the closest approach is in the first or fourth quadrant. The negative torque from the clump at this moment is large, because the gravity of the clump reaches its peak value at this point. Usually, this negative torque is large enough to make the whole time integral of the torque negative, so the  $L_z$  change becomes negative. When calculating the average  $L_z$  changes for all orbits in this panel, the value is positive, as most clump tracks do not go around the star. As we see in Figure 9, the average  $L_z$  change at the clump incoming angle of  $120^\circ$  is indeed positive.

Clump paths in the right panel of Figure 14 give similar results. Most tracks are in the first and fourth quadrants, in accordance with the local shearing sheet model. When the clump path envelops the star, the  $L_z$  change switches from negative to positive. Since most

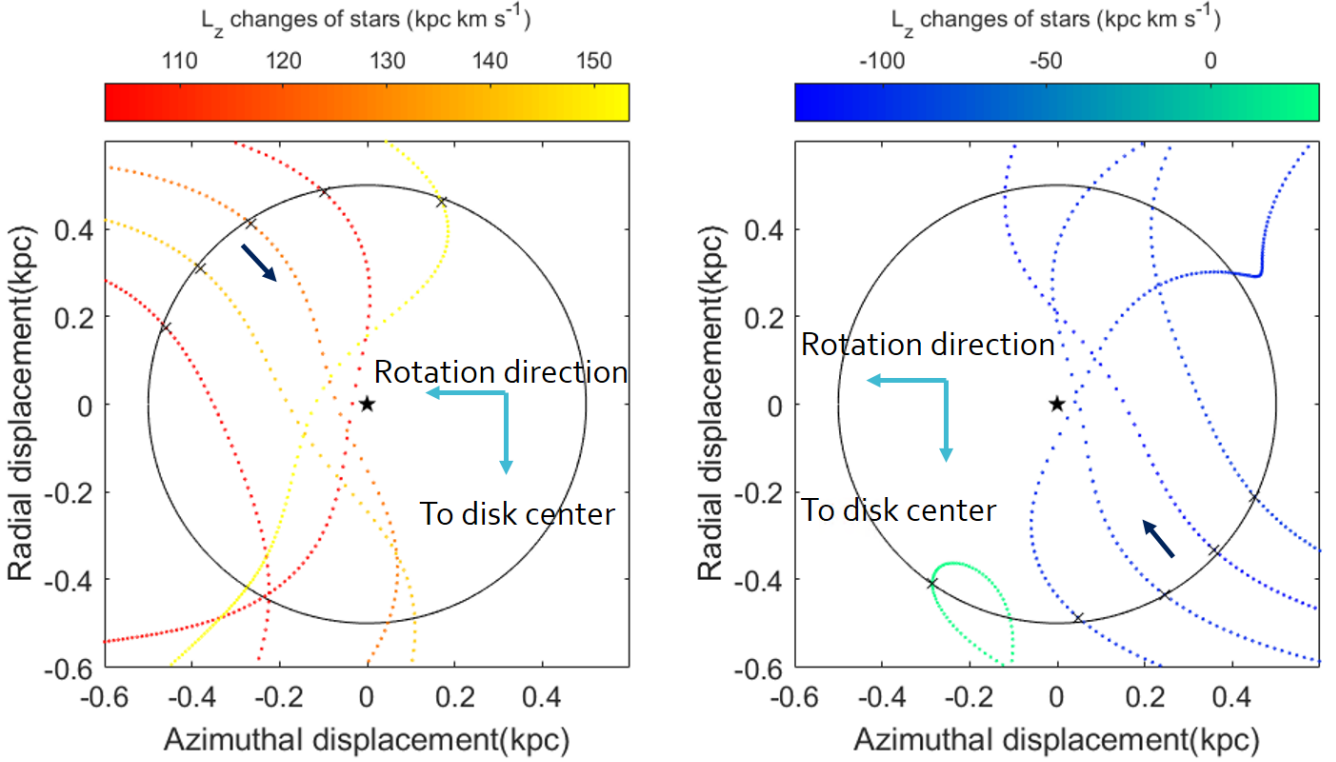


**Figure 13.** Clump positions in the moving frame centred on the star, shown for cases in Figure 12. The black pentagram at the centre is the position of the star. Dotted curves are positions of the clump observed every 1.96 Myr. Black crosses mark the positions where the clump enters the star neighbourhood. Black arrows show the direction of clump motions in this frame. On each panel, downwards is the direction to the galactic centre, and left is the direction of disc rotation. On the left panel, the five tracks ordered by their entrance points from left to right correspond to clump galactic radii  $R_0$  of 8.4, 8.5, 8.6, 8.7, 8.8 kpc, respectively. On the right panel, the five tracks ordered by their entrance points from right to left correspond to clump galactic radii  $R_0$  of 7.6, 7.5, 7.4, 7.3, 7.2 kpc, respectively. The color of dotted curves indicates the  $L_z$  change of the star.

of the tracks do not envelop the star, the average  $L_z$  change for all orbits is negative. This matches the  $L_z$  change value at  $-60^\circ$  on the right panel of Figure 9.

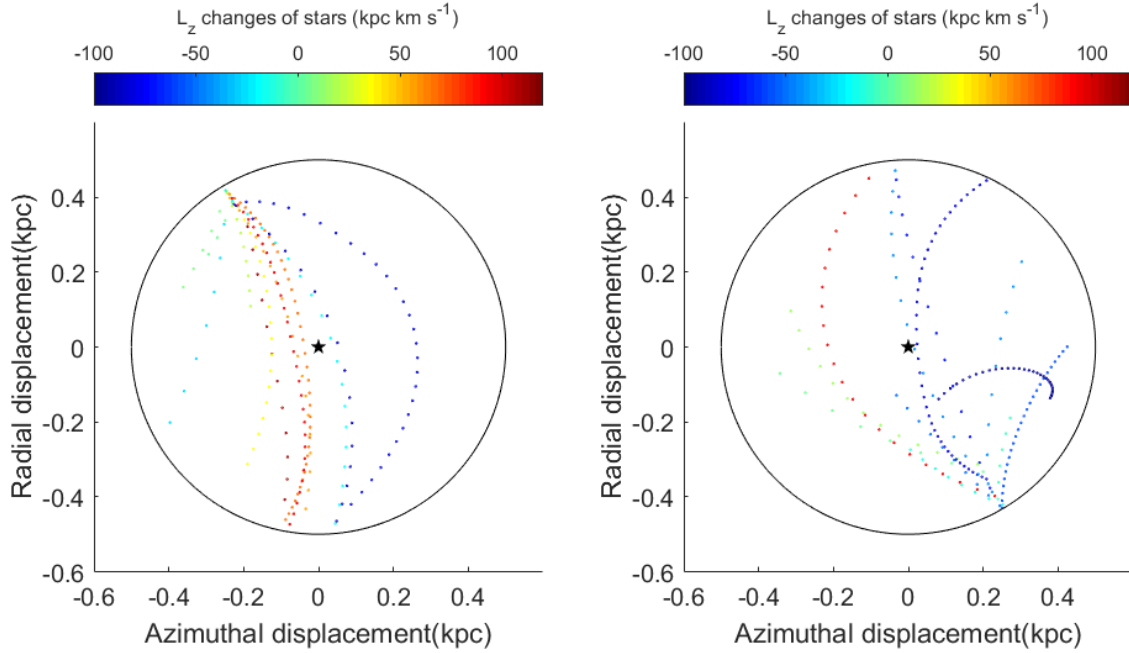
The left and the right panels of Figure 15 show the clump paths and the  $L_z$  changes for encounters with clump incoming angles of  $30^\circ$  and  $-150^\circ$ , respectively, in the simulated galaxy. Since these two clump incoming angles are in the forbidden intervals, the number of orbits in this figure is less than that in Figure 14. On the left panel, almost all the clump tracks go around the star, which is different from what we see in Figure 14. On the right panel, the dark red curve above the star and the yellow curve under the star both have positive  $L_z$  changes. It seems that whether or not a curve goes around a star does not affect the sign of  $L_z$  change here. Another difference is that the clump position at the closest approach in Figure 15 usually has a direction closer to the radial direction, rather than the azimuthal direction. This makes the torque at the closest approach weaker. As a result, the magnitude of  $L_z$  change for each orbit is less than that in Figure 14 on average. On the left panel, the closest approaches of most clump tracks are in the right semicircle, so the average  $L_z$  change at the angle of  $30^\circ$  is negative. On the right panel, the closest approaches of most clump tracks are in the left semicircle, so the average  $L_z$  change at the angle of  $-150^\circ$  is positive. These results agree with the average  $L_z$  change curves in Figure 9.

Figure 16 shows the  $J_r$  changes for the encounter events in Figure 14. Since the  $J_r$  changes depend not only on the net radial impulse from the clump but also on the direction of initial radial

momentum of the star, orbits with similar clump tracks can have different  $J_r$  changes. For example, the orange curve and the dark blue curve on the left panel overlap, but they have totally different  $J_r$  changes. Also on the left panel, whether or not a curve envelops the star does not seem to affect the  $J_r$  change. In the figure, orbits with a large  $J_r$  change are not symmetric about the azimuthal axis across the star. This aligns with our earlier argument during the discussion on the  $J_r$  changes in the local shearing sheet model.

Figure 17 shows the  $J_r$  changes for the encounters at the angle of  $30^\circ$  and  $-150^\circ$ . In this figure, curves are far from symmetric about the azimuthal axis, as most clump positions are in the bottom semicircle. Therefore, the star receives a relatively large net radial impulse, indicating a large  $J_r$  change. As shown on the  $J_r$  curve on Figure, the average  $J_r$  changes at the angles of  $30^\circ$  and  $-150^\circ$  are greater than those at  $120^\circ$  and  $-60^\circ$ .

In summary, the clump incoming angle determines where the clump path is located in the 0.5 kpc circle. The path tells the magnitude and the direction of the stellar acceleration due to the gravity of the clump. When the clump incoming angle is  $0^\circ$ , the distribution of clump paths has most of the clump positions in the right semicircle as all paths start from the right end of the 0.5 kpc circle. This gives a large negative average  $L_z$  change. When the clump incoming angle is  $180^\circ$ , the opposite is true and this case corresponds to a large positive average  $L_z$  change. Individual clump paths in the  $0^\circ$  and  $180^\circ$  cases are far from symmetric about the azimuthal axis. Therefore, both cases have a large  $J_r$  change. When the clump incoming angle



**Figure 14.** Face-on view of clump positions in the moving frame centred on the star, shown for encounters occurring at 8 kpc in the simulated galaxy with clump incoming angles around  $120^\circ$  and  $-60^\circ$ . The black pentagram at the centre is the position of the star. Dotted curves are positions of the clump observed every 1.96 Myr. On each panel, downwards is the direction to the galactic centre, and left is the direction of disc rotation. The left panel and the right panel show clump incoming angles of  $120^\circ$  and  $-60^\circ$ , respectively. The color of dotted curves indicates the  $L_z$  change of the star.

is close to  $90^\circ$  or  $-90^\circ$ , the  $L_z$  change of an individual path usually has a large magnitude. However, as the sign of the  $L_z$  change depends on whether the path goes around the star and both types have similar probability of occurrence, the average  $L_z$  change is close to 0. Because many clump paths are roughly symmetric about the azimuthal axis, the average  $J_r$  changes at  $90^\circ$  and  $-90^\circ$  are close to 0 as well. The above analysis explains the general features shown on the  $L_z$  curve in Figure 9 and the  $J_r$  curve in Figure 10. Angles corresponding to a large average  $L_z$  change, regardless of the sign, also tend to give a large average  $J_r$  change.

As an aside we note that these changes in star-clump collisions are not captured by the impulse approximation. Using the impact parameter and relative velocities of the each collision we computed the change in velocity components predicted by that approximation. We found no significant correlation with the calculated velocity changes. To illustrate this point, it is worth revisiting the left panel of Figure 12, which shows a few stellar trajectories relative to the clump. By looking at the space between adjacent dots, one can find that the difference of the in and out speed at the black circle depends on trajectories and can be positive, negative, or almost 0. This result is inconsistent with the impulse approximation. The looping orbits relative to the clump show that Coriolis forces are important, and therefore the galactic potential is making the impulse approximation oversimplified.

## 4.2 Dependence of $L_z$ changes on clump density distribution

So far, we have provided explanations for the shape of curves on the right panel of Figure 9 and the left panel of Figure 10. In this subsection, we study the influence of clump density profile on the clump incoming angle distribution, which is shown on the left panel of Figure 9. Other factors, such as velocity dispersion, azimuthal drift of stars due to relatively high velocity dispersion, etc., can also affect the distribution of clump incoming angles. Here, we constrain ourselves to clump density profile.

We use the local shearing sheet model to investigate star-clump encounters under different clump surface distributions. We choose the clump density profile to have the following power law surface density distribution

$$\Sigma_{\text{clump}}(r) \propto r^\alpha, \quad (15)$$

where the power  $\alpha$  is a negative constant. Notice that the number of clumps  $n_{\text{clump}}(r)$  in the radial interval  $[r, r+dr]$  satisfies the following

$$n_{\text{clump}}(r) \propto \Sigma_{\text{clump}}(r)rdr \propto r^{\alpha+1}dr. \quad (16)$$

Figure 18 illustrates how we set up the initial conditions for the local shearing sheet model in this case. A star is initially placed at the galactic radius of 8 kpc, shown as the red cross on the left panel. The azimuthal component of the initial velocity of the star follows a normal distribution with a mean of  $113 \text{ km s}^{-1}$  and a standard deviation of  $13 \text{ km s}^{-1}$ . The radial component of the initial

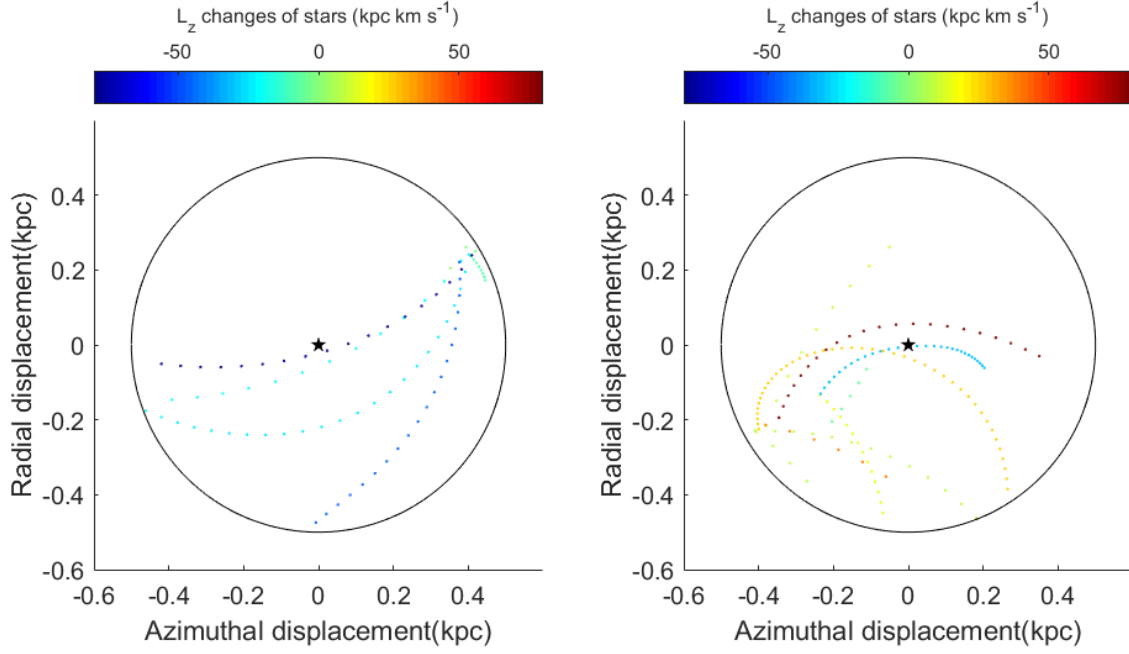


**Figure 15.** Face-on view of clump positions in the moving frame centred on the star, shown for encounters occurring at 8 kpc in the simulated galaxy with clump incoming angles around  $30^\circ$  (left panel) and  $-150^\circ$  (right panel).

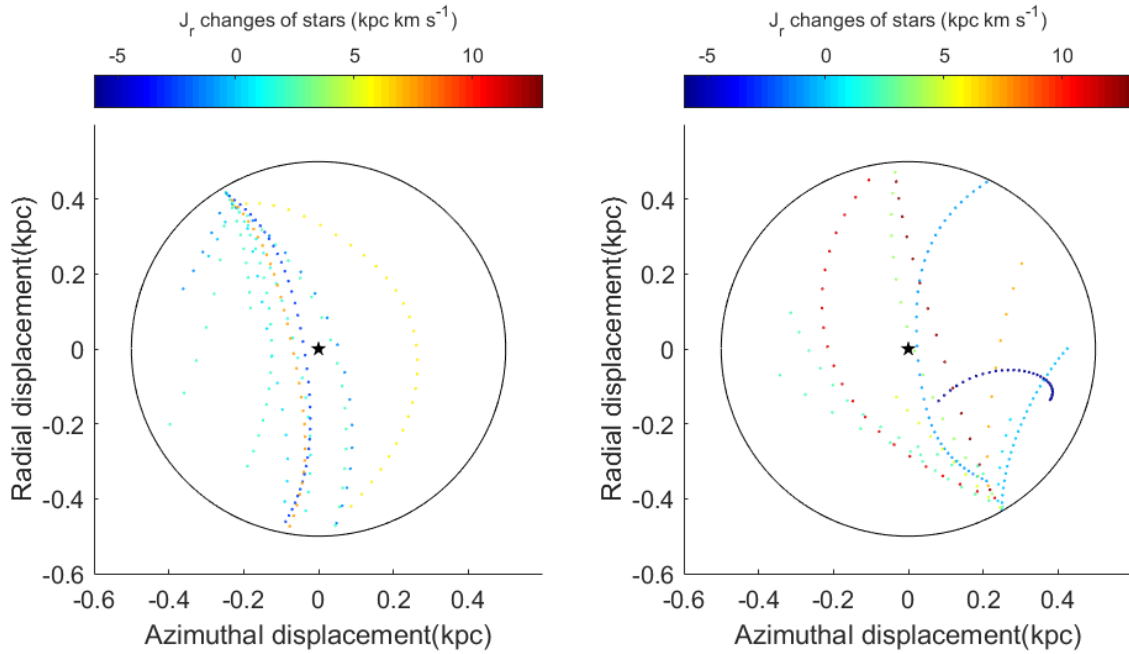


**Figure 16.**  $J_r$  changes for trajectories in Figure 14. The left panel and the right panel show clump incoming angles of  $120^\circ$  and  $-60^\circ$ , respectively. The color of dotted curves indicates the  $J_r$  change of the star.

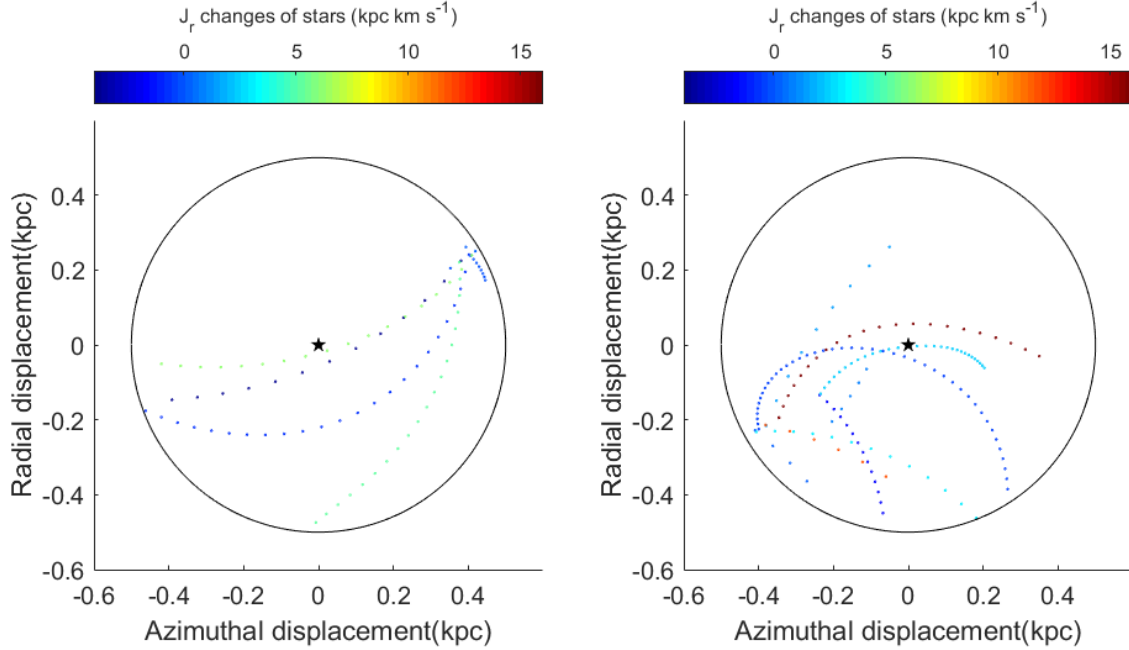


**Figure 17.**  $J_r$  changes for trajectories in Figure 15. The left panel and the right panel show clump incoming angles of  $30^\circ$  and  $-150^\circ$ , respectively. The color of dotted curves indicates the  $J_r$  change of the star.

velocity follows a normal distribution with a mean of  $0 \text{ km s}^{-1}$  and a standard deviation of  $13 \text{ km s}^{-1}$ . As we mentioned before,  $113 \text{ km s}^{-1}$  is the mean rotational speed of stars at 8 kpc in the N-body simulation.  $13 \text{ km s}^{-1}$  is the radial velocity dispersion at 8 kpc in the simulation. A clump is initially placed in an annular sector, shown by the solid lines on the left panel. The azimuthal span  $\psi$  of the annular sector is  $48^\circ$ , with the star at the centre. The radial interval of the annular sector is from 7 kpc to 9 kpc. In this annular sector, the initial position of the clump follows a uniform distribution in the azimuthal direction and a power law distribution described by Equation 16 in the radial direction. The velocity of the clump is always  $113 \text{ km s}^{-1}$  along the azimuthal direction.

After an initial velocity of the star and an initial position of the clump are determined, the motion of the star in the rotating frame centred on the clump is calculated by the local shearing sheet model. For example, if the initial velocity of the star is  $113 \text{ km s}^{-1}$  along the azimuthal direction and the initial position of the clump is at the blue dot on the left panel, the path of the star in the clump frame will be the orange curve in the right panel. Here, the blue dot represents the position of the clump. The red cross is the initial position of the star. The horizontal and vertical axis stand for azimuthal displacement and radial displacement, respectively. In this panel, downwards is the direction to the galactic centre, and left is the direction of disc rotation. To obtain the clump incoming angle, one needs to view the orbit as the trajectory of the clump in the moving frame centred on the star. Since this conversion has been shown in the previous subsection, we do not present it here.

To figure out the distribution of clump incoming angles, we run the local shearing sheet model 60 000 times for each clump surface density distribution. Among the 60 000 samples, we only count those where the star can enter the clump neighbourhood within 1

**Table 3.** Mean stellar  $L_z$  changes during encounters and the frequency ratio of negative clump incoming angles to positive ones under clump density profiles with different power  $\alpha$  in Equation 15. Encounters are generated using the local shearing sheet model at the galactic radius of 8 kpc.

Power $\alpha$	Mean $L_z$ change ( $\text{kpc km s}^{-1}$ )	$n_-/n_+$
-0.5	$2.99 \pm 0.49$	0.919
-1.5	$0.94 \pm 0.49$	0.964
-2.5	$-0.03 \pm 0.48$	1.051
-3.5	$-0.66 \pm 0.49$	1.108
-4.5	$-0.84 \pm 0.49$	1.129
-5.5	$-1.62 \pm 0.49$	1.215
-6.5	$-2.64 \pm 0.49$	1.231

Gyr. Let  $n_+$  and  $n_-$  denote the number of encounters with positive clump incoming angles and negative clump incoming angles, respectively. Table 3 shows the mean  $L_z$  changes and the  $n_-/n_+$  ratios for clump distributions with different power  $\alpha$ . As one can see, the mean  $L_z$  change decreases and the  $n_-/n_+$  ratio increases as the power  $\alpha$  in Equation 15 goes from -0.5 to -6.5. When the power  $\alpha$  goes down, the clump surface density function favours small radii to a larger degree, and more clumps get distributed closer to the inner arc of the annular sector. As more clumps are initially placed at a galactic radius less than the star, the star is more likely to approach the clump from a higher orbit, which leads to an encounter with a negative clump incoming angle. Therefore, the  $n_-/n_+$  ratio increases. From Figure 13, we know that a positive clump incoming angle usually gives a positive  $L_z$  change and a negative angle usually gives a negative  $L_z$  change. As the  $n_-/n_+$  ratio increases, it is natural to see that the mean  $L_z$  change falls.

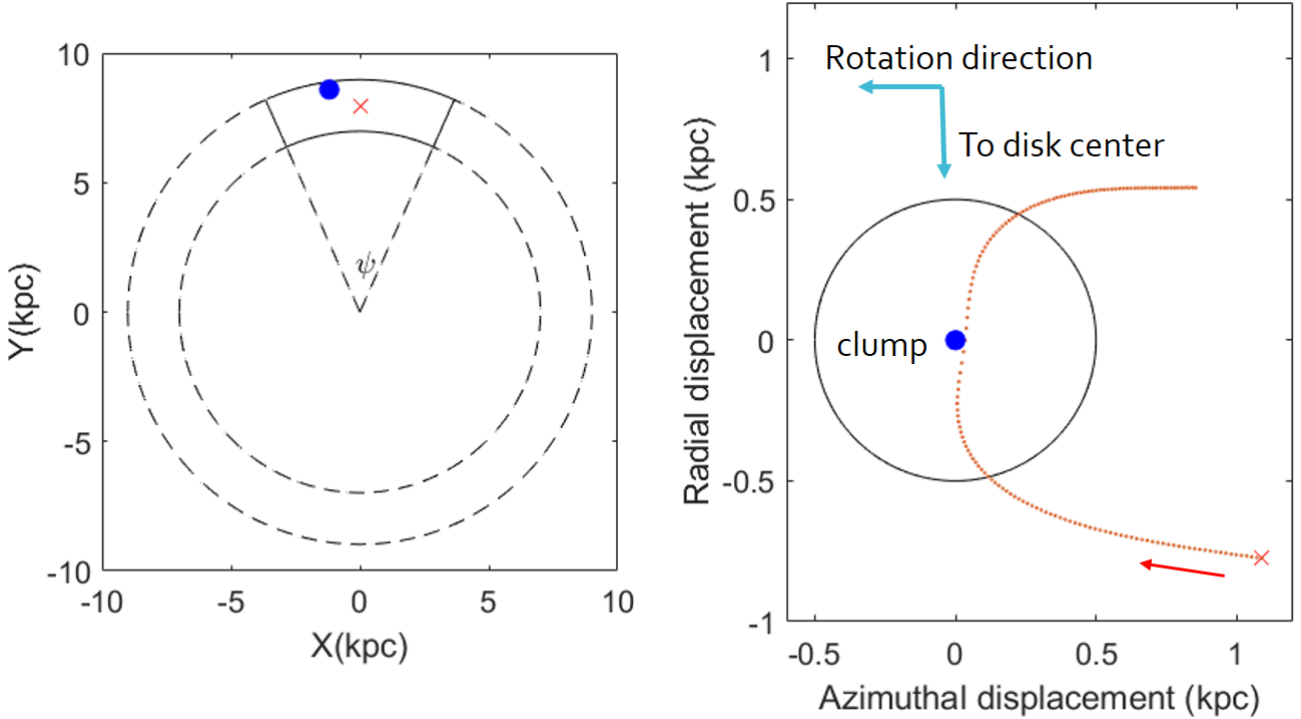


**Figure 18.** Demonstration of the initial condition setup in the local shearing sheet model. The left panel is the face-on view of the galaxy with the galactic centre at the origin. In the model, the initial position of the star, represented by the red cross, is placed at (0, 8). The initial position of the clump is constrained in the annular sector with the angle  $\psi$  of  $48^\circ$  and the two arcs at 7 kpc and 9 kpc. After the initial position of the clump, represented by the blue dot, is determined on the left panel, we calculate the orbits of the star in the rotating frame centred on the clump, shown as the dotted curve on the right panel. On the right panel, the horizontal axis and the vertical axis represent azimuthal displacement and radial displacement, respectively. Downwards is the direction to the galactic centre, and left is the direction of disc rotation, which is the same as Figure 12. The red arrow shows the direction of the stellar motion in this frame.

Figure 19 shows the clump contact angle distribution and the average  $L_z$  change in each angle bin for several clump surface density profiles. If the initial velocity of the star does not carry any random orbital energy, the regular intervals of clump incoming angles are  $[70^\circ, 160^\circ]$  and  $[-125^\circ, -25^\circ]$  as shown on Figure 13, corresponding to two types of cases where the star approaches the clump from a smaller galactic radius and a greater galactic radius, respectively. On the left panel of Figure 19, the frequencies in the first regular interval generally go up and the ones in the second go down as the power  $\alpha$  decreases. This confirms the explanation given in the previous paragraph. When looking at the two local maximum points of each distribution curve, the left local maximum frequency gradually rises and the right one declines as the power goes down. The left peak is shorter than the right peak at the power of -0.5, and the opposite holds at the power of -6.5.

As mentioned before, the initial clump surface density in the simulated galaxy follows  $e^{-r^2/h^2}$  with a scale length of  $h = 5.4$  kpc. The ratio of the density at 7 kpc to the density at 9 kpc is 3.00, which corresponds to a power  $\alpha$  of -4.37. This power will give a mean  $L_z$  change of  $-0.82$  kpc km s $^{-1}$  when using values at  $\alpha = -3.5$  and  $\alpha = -4.5$  in Table 3 with a linear interpolation. If we compare it to the mean  $L_z$  change at 8 kpc in Table 2, the two numbers are compatible considering the uncertainties. When comparing the incoming angle frequency curve at 8 kpc in Figure 9 to the frequency curve at  $\alpha = -4.5$  in Figure 19, they do not match very well. Besides the difference in clump surface density profiles, the curve of the simulated galaxy

is under the influence of stellar motions in the  $z$ -direction, and the azimuthal drift due to stellar velocity dispersion makes stars have a smaller mean rotational speed than the clumps. These may be the sources of the divergence.

The result presented so far on the dependence of  $L_z$  changes on the clump density distribution is obtained from the local shearing sheet model. To verify this dependence, we run another GADGET-2 simulation where the initial clump surface density follows a power law with  $\alpha = -0.5$  and all the other parameters are the same as those in the middle column of Table 1. Table 4 shows the mean  $L_z$  change of a star when it encounters with a clump in this new simulation. One can see that the mean  $L_z$  change is positive for  $r > 5$  kpc, so the change in the clump profile flips the sign of  $L_z$  changes. At  $r = 8$  kpc, the mean  $L_z$  change is  $2.89 \pm 0.32$  kpc km s $^{-1}$ , which agrees with the value for  $\alpha = -0.5$  in Table 3. As for  $r \leq 5$  kpc, the mean  $L_z$  changes there are close to values in Tables 2. This is mainly because the clump density gradient at  $r \leq 5$  kpc in the original simulation is not far away from a power law with  $\alpha = -0.5$ . For example, with an  $e^{-r^2/h^2}$  clump profile and  $h = 5.4$  kpc, the ratio of the clump density at 2 kpc to the density at 4 kpc in the original simulation is 1.51. In the new simulation with a  $1/\sqrt{r}$  clump profile, this ratio is 1.41, very close to 1.51.

Figure 20 shows the distributions of clump incoming angles and the dependence of  $L_z$  changes on the angles in the new simulations. When comparing the left panel with that of Figure 9, one can find that the new simulation has a larger frequency in the angle inter-

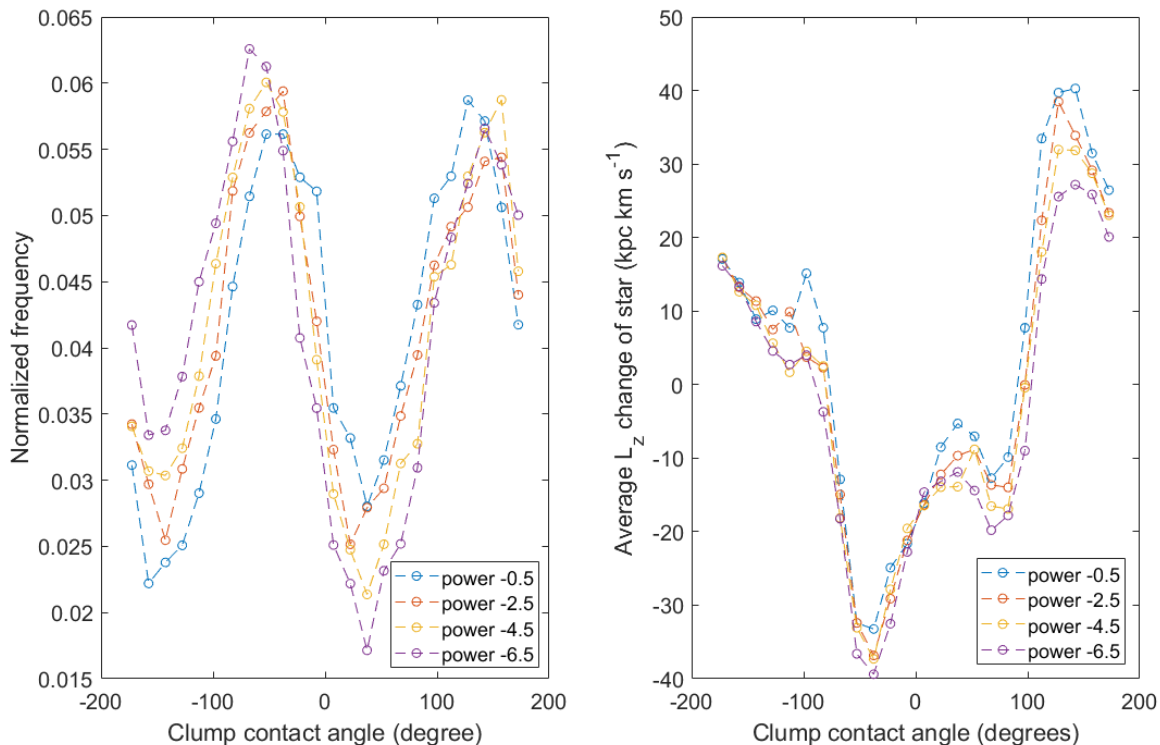


**Figure 19.** The distribution of clump incoming angles and average  $L_z$  changes as a function of clump incoming angles for clump density profiles with different power  $\alpha$ . Encounters are generated using the local shearing sheet model at the galactic radius of 8 kpc. The bin width in both panels is 15 degrees.

**Table 4.** The mean  $L_z$  change of a star during one encounter with a clump at different Galactic radii in the GADGET-2 run starting with a  $1/\sqrt{r}$  clump surface density. The  $L_z$  change is calculated using the  $L_z$  value when a star enters a circle of 0.5 kpc radius around a clump and the one when the star goes out of the circle.

Galactic radius (kpc)	Mean $L_z$ change (kpc km s $^{-1}$ )	Average number of encounters per star in one gigayear
1	$0.07 \pm 0.01$	46.2
2	$-0.31 \pm 0.03$	28.7
3	$-0.45 \pm 0.05$	17.8
4	$-0.08 \pm 0.08$	14.3
5	$-0.25 \pm 0.10$	10.7
6	$1.98 \pm 0.17$	11.2
7	$1.49 \pm 0.24$	10.1
8	$2.89 \pm 0.32$	8.5
9	$4.12 \pm 0.49$	5.3
10	$1.49 \pm 0.99$	2.3

val of  $[70^\circ, 160^\circ]$ . As this angle range corresponds to events where a star meets a clump that has a slightly larger orbital radius than the star, this confirms the result that a shallower clump gradient makes stars more likely to approach a clump from a lower orbit, which has been shown on Figure 19. Overall, results from the new simulation are consistent with the findings of the shearing sheet model.

Although the initial clump profile gets changed in the new simulation, the stellar surface density profile still evolves from  $e^{-r^2/h^2}$  to an exponential as the original simulation. Figure 21 shows the sec-

ond derivative of the logarithm of stellar surface density as a function of time. Similar to the curve in Figure 4, the second derivative gradually increases from a negative value to zero, which indicates an exponential profile. Even though the  $L_z$  changes in the outer disc show an outwards bias, this run still produces an exponential stellar profile. An inwards scattering bias is not a prerequisite for the formation of an exponential.

## 5 DISCUSSION AND CONCLUSIONS

The analysis of a self-gravitating disc shows that star-clump encounters in a galactic disc where hundreds of massive objects exist can contribute to more than 95% of large stellar angular momentum changes, which drive the surface density profile to evolve towards an exponential shape. The rate of profile evolution has a positive correlation with the frequency of star-clump encounters. In the simulated galaxy, both the evolution rate and the encounter frequency tend to decline with time, as the stellar disc thickens and clumps fall into the galactic centre.

Besides angular momentum, star-clump encounters can also alter the radial action and the vertical action of the involved star. An average encounter event increases the star's radial action and vertical action, leading to manifest disc heating. Velocity changes in the scattering events are not well approximated by the classical Impulse Approximation. These results generally agree with those of Spitzer & Schwarzschild (1953) and Hänninen & Flynn (2002). They differ somewhat from the results of D'Onghia et al. (2013) and Vera-Ciro et al. (2016) which find little vertical heating. The more massive

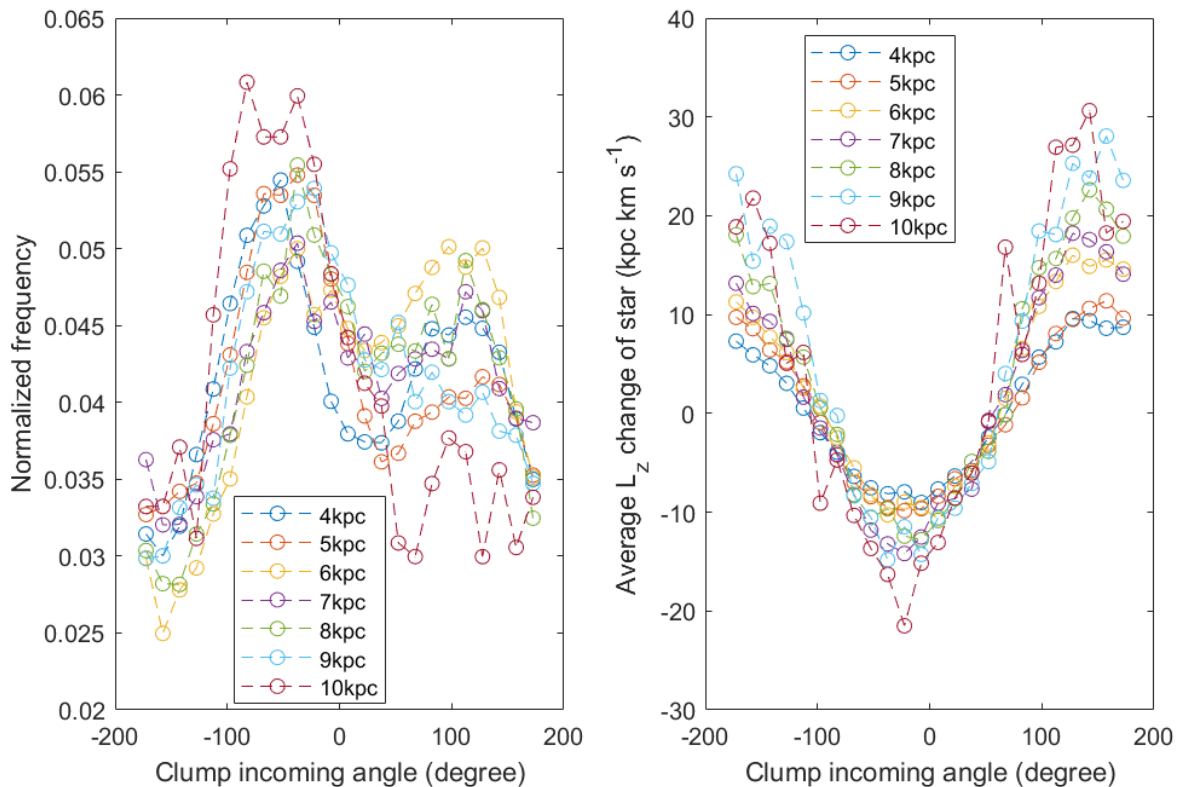


**Figure 20.** The distribution of clump incoming angles and average  $L_z$  changes as a function of clump incoming angles in the GADGET-2 run starting with a  $1/\sqrt{r}$  clump surface density. Colors reflect encounters occurring at different galactic radii. The bin width in both panels is 15 degrees.

clumps in the present models scatter more strongly and affect stars at greater distances. Moreover, these more massive clumps move radially through the stellar disc and stellar orbits get more eccentric after initial scattering events, with both effects enhancing scattering.

Detailed analysis on stellar orbits shows that the angular momentum change and the radial action change during an encounter depend on the direction from which a star approaches a clump. A star that enters the neighbourhood of a clump from a greater galactic radius is more likely to lose angular momentum, and one that goes into the clump neighbourhood from a smaller radius has more chance to gain. The radial action change is more pronounced when a star approaches a clump along the azimuthal direction, and less when the approach is along the radial direction.

The mean angular momentum change of stars during encounter events can be affected by the surface density distribution of the clumps. In a region where the clump density falls quickly with radius, stars are more likely to meet a clump which has a lower orbit, which causes the mean angular momentum change to be negative. In a region where the clump density falls slowly, the mean angular momentum change can be positive. Simulations show that either type of the clump distribution can generate an exponential disc through stellar scattering. Therefore, the origin of an exponential is independent of the sign of angular momentum changes. [Elmegreen & Struck \(2016\)](#) showed how an exponential is reached when an inward scattering bias is present in a disc. Future theoretical work should be done on why an exponential can emerge from scatterings with no bias or with an outward bias.

## DATA AVAILABILITY

The data used in this article will be shared on request to the corresponding author.

## REFERENCES

- Binney J., 2012, *MNRAS*, **426**, 1324  
 Binney J., Tremaine S., 2008, *Galactic Dynamics: Second Edition*. Princeton Univ. Press  
 Bouquin A. Y. K., et al., 2018, *ApJS*, **234**, 18  
 Burstein D., 1979, *ApJ*, **234**, 829  
 Comerón S., et al., 2012, *ApJ*, **759**, 98  
 D’Onghia E., Vogelsberger M., Hernquist L., 2013, *ApJ*, **766**, 34  
 Dalcanton J. J., Yoachim P., Bernstein R. A., 2004, *ApJ*, **608**, 189  
 Daniel K. J., Wyse R. F. G., 2018, *MNRAS*, **476**, 1561  
 Dormand J. R., Prince P. J., 1980, *J. Comp. Appl. Math.*, **6**, 19–26  
 Elmegreen B. G., Elmegreen D. M., 2006, *ApJ*, **650**, 644  
 Elmegreen B. G., Struck C., 2013, *ApJ*, **775**, L35  
 Elmegreen B. G., Struck C., 2016, *ApJ*, **830**, 115  
 Elmegreen B. G., Struck C., Hunter D. A., 2014, *ApJ*, **796**, 110  
 Ferguson A. M. N., Clarke C. J., 2001, *MNRAS*, **325**, 781  
 Freeman K. C., 1970, *ApJ*, **160**, 811  
 Hänninen J., Flynn C., 2002, *MNRAS*, **337**, 731  
 Hernquist L., 1990, *ApJ*, **356**, 359  
 Herrmann K. A., Hunter D. A., Elmegreen B. G., 2013, *AJ*, **146**, 104  
 Hohl F., 1971, *ApJ*, **168**, 343  
 Hunter D., Elmegreen B. G., 2006, *ApJS*, **162**, 49  
 Julian W. H., Toomre A., 1966, *ApJ*, **146**, 810

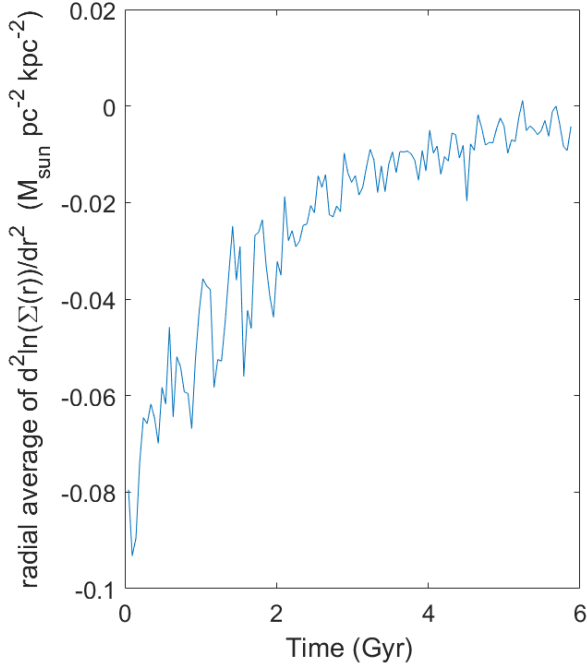


**Figure 21.** Time evolution of the second derivative of the logarithm radial stellar profile in the GADGET-2 run starting with a  $1/\sqrt{r}$  clump surface density. The radial average is taken from 2 kpc to 9 kpc.

- Lin D. N. C., Pringle J. E., 1987, *ApJ*, **320**, L87  
Mestel L., 1963, *MNRAS*, **126**, 553  
Naab T., Ostriker J. P., 2017, *ARA&A*, **55**, 59  
Pohlen M., Trujillo I., 2006, *A&A*, **454**, 759  
Sellwood J. A., Binney J. J., 2002, *MNRAS*, **336**, 785  
Shampine L. F., Reichelt M. W., 1997, *SIAM Journal on Scientific Computing*, **18**, 1–22  
Shu F. H., 2016, *ARA&A*, **54**, 667  
Spitzer Lyman J., Schwarzschild M., 1951, *ApJ*, **114**, 385  
Spitzer Lyman J., Schwarzschild M., 1953, *ApJ*, **118**, 106  
Springel V., 2005, *MNRAS*, **364**, 1105  
Staudaer S. M., Dale D. A., van Zee L., 2019, *MNRAS*, **486**, 1995  
Struck C., Elmegreen B. G., 2017a, *MNRAS*, **464**, 1482  
Struck C., Elmegreen B. G., 2017b, *MNRAS*, **469**, 1157  
Struck C., Elmegreen B. G., 2019, *MNRAS*, **489**, 5919  
Toomre A., 1964, *ApJ*, **139**, 1217  
Vasiliev E., 2019, *MNRAS*, **482**, 1525  
Vera-Ciro C., D’Onghia E., Navarro J., Abadi M., 2014, *ApJ*, **794**, 173  
Vera-Ciro C., D’Onghia E., Navarro J. F., 2016, *ApJ*, **833**, 42  
Wielen R., 1977, *A&A*, **60**, 263  
Williams J. P., McKee C. F., 1997, *ApJ*, **476**, 166  
Wu J., Struck C., D’Onghia E., Elmegreen B. G., 2020, *MNRAS*, **499**, 2672  
Yoachim P., Dalcanton J. J., 2006, *AJ*, **131**, 226  
van der Kruit P. C., Searle L., 1981, *A&A*, **95**, 105

This paper has been typeset from a  $\text{\TeX}/\text{\LaTeX}$  file prepared by the author.